



HAL
open science

Offshore Mayotte volcanic plumbing revealed by local passive tomography

Océane Foix, Chastity Aiken, Jean-Marie Saurel, Nathalie Feuillet, Stephan Jorry, Emmanuel Rinnert, Isabelle Thinon

► To cite this version:

Océane Foix, Chastity Aiken, Jean-Marie Saurel, Nathalie Feuillet, Stephan Jorry, et al.. Offshore Mayotte volcanic plumbing revealed by local passive tomography. *Journal of Volcanology and Geothermal Research*, 2021, 420, pp.107395. 10.1016/j.jvolgeores.2021.107395 . insu-03466310

HAL Id: insu-03466310

<https://insu.hal.science/insu-03466310>

Submitted on 2 Mar 2022

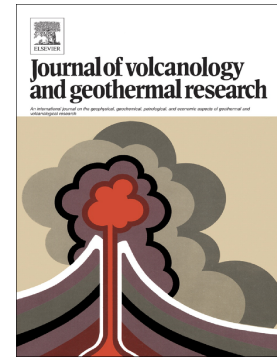
HAL is a multi-disciplinary open access archive for the deposit and dissemination of scientific research documents, whether they are published or not. The documents may come from teaching and research institutions in France or abroad, or from public or private research centers.

L'archive ouverte pluridisciplinaire **HAL**, est destinée au dépôt et à la diffusion de documents scientifiques de niveau recherche, publiés ou non, émanant des établissements d'enseignement et de recherche français ou étrangers, des laboratoires publics ou privés.

Journal Pre-proof

Offshore Mayotte volcanic plumbing revealed by local passive tomography

Océane Foix, Chastity Aiken, Jean-Marie Saurel, Nathalie Feuillet, Stephan J. Jorry, Emmanuel Rinnert, Isabelle Thinon, MAYOBS/REVOSIMA Seismology Team



PII: S0377-0273(21)00224-9

DOI: <https://doi.org/10.1016/j.jvolgeores.2021.107395>

Reference: VOLGEO 107395

To appear in: *Journal of Volcanology and Geothermal Research*

Received date: 4 March 2021

Revised date: 8 September 2021

Accepted date: 11 September 2021

Please cite this article as: O. Foix, C. Aiken, J.-M. Saurel, et al., Offshore Mayotte volcanic plumbing revealed by local passive tomography, *Journal of Volcanology and Geothermal Research* (2021), <https://doi.org/10.1016/j.jvolgeores.2021.107395>

This is a PDF file of an article that has undergone enhancements after acceptance, such as the addition of a cover page and metadata, and formatting for readability, but it is not yet the definitive version of record. This version will undergo additional copyediting, typesetting and review before it is published in its final form, but we are providing this version to give early visibility of the article. Please note that, during the production process, errors may be discovered which could affect the content, and all legal disclaimers that apply to the journal pertain.

© 2021 Elsevier B.V. All rights reserved.

Offshore Mayotte Volcanic Plumbing Revealed by Local Passive Tomography

Authors List:

- **Océane Foix**¹ (oceane.foix@ifremer.fr)
- Chastity Aiken¹ (chastity.aiken@ifremer.fr)
- Jean-Marie Saurel² (saurel@ipgp.fr)
- MAYOBS/REVOSIMA Seismology Team (seismo_mayotte@services.cnrs.fr)
- Nathalie Feuillet² (feuillet@ipgp.fr)
- Stephan J. Jorry¹ (stephan.jorry@ifremer.fr)
- Emmanuel Rinnert¹ (emmanuel.rinnert@ifremer.fr)
- Isabelle Thinon³ (i.thinon@brgm.fr)

¹ IFREMER, Unité Géosciences Marines, Technopole La Pointe du Diable, 29280 Plouzané, France

² Université de Paris, Institut de physique du globe de Paris - CNRS, F-75005 Paris, France

³ BRGM-French geological survey, DGR/GBS, F-45060 Orléans, France

Corresponding author:

Océane Foix : oceane.foix@ifremer.fr (previous e-mail address)

foixoceane@hotmail.fr (permanent e-mail address)

Ifremer - Centre de Bretagne

Géosciences Marines, Laboratoire Aléas et Dynamique Sédimentaire

1625 Route de Sainte Anne

29280 Plouzané France

Abstract.

A new submarine volcano has been discovered offshore Mayotte, a part of the Comoros volcanic archipelago located between Africa and Madagascar. The edifice arose from the sea-

floor following a seismo-volcanic crisis that started in May 2018. This seismo-volcanic activity highlights very deep magma reservoirs and dykes in the East Mayotte volcanic system. Since the crisis, the region has experienced $> 2,000$ earthquakes with magnitude ≥ 3.5 and activity continues today (August 17, 2021). The earthquakes are unusually deep and distributed into two swarms: one 5-15 km east of Petite-Terre at 25-55 km depth and a second 25 km away at 30-50 km depth. Significant subsidence of Mayotte to the East has been assigned to the drainage of a deep magma chamber, inferred to be located 30 km from the coast. However, at present, the earthquake locations and geodetic observations have not been sufficient to image entirely the structure of the volcanic plumbing system. In this study, we construct V_p , V_s , dV_p , dV_s and V_p/V_s 3D velocity models to assess the deeper structure of the young volcano plumbing system, offshore and East of Mayotte. Using $> 3,000$ earthquakes from an ongoing monitoring effort, and a 1D velocity model determined onboard, we jointly inverted for velocity structures, earthquake locations, origin times, and station corrections using LOTOS software. The calculated 3D velocity models highlight a complex volcanic system down to 40 km depth. Specifically, we image 3 interpreted reservoirs, more or less consolidated/old. The main reservoir is located at about 30 km depth and deeper, making it one of the deepest magmatic chamber imaged. The reservoirs are connected by several old crystallized conduits, whose existence could have been influenced by the presence of an old fracture zone, globally oriented $N130^\circ$, due to a regional strike-slip motion of the lithosphere. Moreover, gas-saturated rock may be present below the currently degassing *Horse Shoe* structure. We were unable to image connections between the new volcanic edifice and reservoirs or conduits due to a lack of resolution in that part of the study area.

Keywords: Earthquake tomography, active volcano, volcano seismology, magma chamber,

Comoros archipelago, Indian Ocean.

Journal Pre-proof

1. Introduction

Deep volcanic systems are not well understood, and seismic imaging them are rare. Some earthquake tomography studies of deep volcanic systems have been conducted along subduction zones, such as the Toba volcano (Koulakov et al., 2009a) and Kamchatka volcanic complex (Koulakov et al., 2020a). Those studies highlighted ascending magma resulting from the dehydration of the subducting plate. It is known that subduction zone volcanic arcs involve crust and mantle multilevel magma-reservoirs (i.e., Dobretsov et al., 2012 and above referees). However, we do not know deep volcanic feeding systems in other geological contexts, such as that of Mayotte. Here, we investigate Mayotte's volcanic system to understand what influences deep volcanic system structure and behavior.

Mayotte is part of the Comoros volcanic archipelago (CVA) located between South Africa and Madagascar, in the Mozambique Channel (figure 1, A). The on-going seismovolcanic crisis highlights a complex system because we do not know its deep crustal structure. Since May 2018, seismicity has continued to occur offshore Mayotte, where a new volcanic edifice (NVE) has been discovered at 50 km to the East of Petite-Terre. The edifice is located at the eastern part of a N130° alignment of volcanic edifices that we label the volcanic ridge (figure 1) (Feuillet et al., 2019; 2021). Early-recorded earthquake sequences (2018-2019) and petrology have provided some understanding of the link between a deep magma chamber and the new volcano (Lemoine et al., 2020; Cesca et al., 2020; Laurent et al., 2020; Berthod et al., 2021). However, we still lack a deeper understanding of the overall volcanic plumbing structure of East Mayotte volcanic ridge (EMVR) in terms of its past and present-day activity.

The Mozambique Channel tectonic regime is influenced by an East-Northeast West-Southwest offshore extension of the East African Rift System (e.g., Deville et al., 2018 and its references). Magmatic activity in the CVA appeared first in Mayotte, ~20 Myr ago, followed by Anjouan, Mohéli, and Grande Comore ~10-11 Myr ago (Nougier et al., 1986; Michon,

2016). The more recent volcanic activity is dated in Grande Comore (Karthala) at 0.13 ± 0.02 Myr to present. The CVA origin is still debated. Emerick and Duncan (1982) proposed the presence of a hot spot, but the inference does not match with velocity models of plate motion and structural features of the region (Famin et al., 2020). It could also be influenced by lithospheric fractures (Nouguier et al., 1986) or result from a combination of both processes (Debeuf, 2004; Michon 2016). A more recent work, based on the current seismo-volcanic crisis, interprets the region as undergoing lithospheric-scale rifting (Feuillet et al., 2021). Several NW-SE ridges and rifts are organized in échelon to transfer the deformation from East-African rift (Feuillet et al., 2021). Famin et al. (2020) interpret the region as a plate limit with dextral motion while Stamps et al. (2020) consider the CVA as the northern extent of a diffuse transtensional zone accommodating the extension between the Somalian and Rovuma plates.

Fig.1. Mayotte volcano-seismic settings. A: Comoros archipelago and Mayotte locations marked by the black rectangle. B: Close-up on the Comoros archipelago and Mayotte Islands. Red triangles are known active volcanoes. C: Close-up on Mayotte Grande-Terre and Petite-Terre islands area. Black triangles represent land and offshore seismic stations available between February and November 2019. Circles illustrate earthquakes distribution recorded by seismic stations, with size proportional to the magnitude and color dependent on depth. Grey patches indicate volcanic cones and ridges with names determined by Feuillet et al. (2021). PSC: Proximal Seismic Cluster. DSC: Distal Seismic cluster. NVE: New volcanic edifice. **[COLOR NEEDED]**

Locally, explosive volcanic eruptions on Grande-Terre and Petite-Terre (Mayotte islands) have been describe. The latest dated tephra on land occurred between 4,000 and 7,000 years, but its origin was not determined (Zinke et al., 2003a; 2003b). At sea, recent activity is evidenced by the presence of several cones on the insular slope (Audru et al., 2006; Famin et al., 2020; Tzevahirtzian et al., 2021; Feuillet et al., 2021). According to the lithospheric-scale rifting of the region, these cones are distributed along a W-NW / E-SE volcanic ridge (N130°) where the NVE (820 m high and ~5 km wide) has been discovered (Feuillet et al., 2021).

Feuillet et al. (2021) highlights the *Horse Shoe* (HS) degassing structure, with a 3.5 km wide cone, and the *Crown*, with a 4 km wide circular structure composed of 100-150 m high volcanic edifices, suggesting post-caldera domes (figure 1, C). A 10 km wide flat depression seems to surround the *Crown*. In addition, the nature of the lithosphere offshore Mayotte to the East is still unknown; its oceanic or continental nature is still debated. Beneath Mayotte island, the depth of the Moho has been estimated to be at 18 km depth in the region based on a receiver function study (Dofal et al., 2018).

For several years, the Mayotte region has been considered as a moderate seismically active area, having produced several M5 events and one event with a maximum magnitude evaluated at 6.1 MLv (Bertil et al., 2018). Since May 2018, the Mayotte inhabitants have felt hundreds of earthquakes. Most are small in magnitude but several moderate-sized events have occurred (monthly report of REVOSIMA, <https://www.ipgp.fr/fr/revosima/actualites-reseau>). On 15 May 2018, a M5.9 event occurred and due to the weakening of structures and previous minor damages from previous earthquakes, induced damages to buildings (Masson et al., 2018). The present-day seismic volcanic crisis has been accompanied by a significant subsidence of Mayotte Island, between 9 and 17 cm (Lemoine et al., 2020; Cesca et al., 2020; Feuillet et al., 2021). This subsidence has been assigned to the drainage of a magma chamber. A number of very low frequency (VLF, 15s oscillation period) events have been recorded and the largest one, recorded worldwide, occurred on 11 November 2018. Its occurrence has been attributed to fluid movement within the volcanic system (Cesca et al., 2020; Laurent et al., 2020; Feuillet et al., 2021). Since 2019, seismicity has been concentrated primarily near Petite-Terre (PSC: Proximal Seismic Cluster, figure 1), at about 5 to 15 km from the coast, and at a depth ranging from 25 to 55 km from the seafloor, below the Moho, with an apparent donut-shaped ring in map view (Jacques et al., 2019; Lavayssière et al., 2020; Feuillet et al., 2021). This activity represents 90% of the present-day located events (Saurel et

al., resubmitted). A secondary seismic cluster of earthquakes (DSC: Distal Seismic Cluster, figure 1) is located 25 km East from Petite-Terre, between 30 to 50 km depth, and shows no clear evidence of a connection to the PSC. From the DSC, a thin N140° seismic region extends toward the NVE with depth appearing to diminish approaching the edifice (Saurel et al., resubmitted).

Thanks to the many oceanographic deployments (MAYOBS series, Feuillet et al., 2019), more than 3,000 earthquakes have been recorded by the land-based network and relocated with the multiple OBS deployed along the EMVR (figure 1). These ~3,000 manually relocated earthquakes provide a unique opportunity to produce a local 3D seismic image of the deep crustal structure beneath the EMVR in the context of present-day earthquake activity (Saurel et al., resubmitted). From the 3D velocity model we produced in this study, we aim to answer the following questions: Are there one or several magmatic reservoirs involved in the East Mayotte volcanic system? Where are they? Is there an influence of the regional tectonic regime on the volcanic plumbing system? Can we image gas related to the volcanic activity? Does the East Mayotte volcanic system have an old volcanic plumbing history, or is it a young, neoformed system?

Using well-resolved earthquake locations, hand-picked earthquake phases, and a 1D velocity model in LOTOS (Local Tomography Software - Koulakov, 2009), we present in this work the first local passive earthquake tomography images of the volcanic plumbing system of East Mayotte, offshore. In the following sections, we detail the local passive tomographic inversion methods we employ to image the East Mayotte volcanic system (EMVS) (Section 2), and our tomographic imaging results along the EMVR (Section 3). We discuss the imaging in the context of known geology and seismicity as well as known topography from bathymetric mapping conducted during the many oceanographic campaigns since 2019 (Section 4). This work provides a detailed structure of the EMVS and provides a deeper understanding

of the larger-scale lithospheric processes involved in the region, from past to present.

2. Passive Local Tomography Inversion

2.1. Networks and input data

MAYOBS is a series of monitoring surveys dedicated to follow the evolution of the seismo-volcanic crisis affecting Mayotte since May 2018. The long-term project includes several successive OBS recoveries and deployments from February 2019 to the present day (Feuillet et al., 2019). Only a local seismic stations network is used for this study, and it is composed of 70 onshore and offshore stations (grey triangles in figure 1 and tables S1 and S2): (1) 10-land seismometers were progressively set up on Petite-Terre and Grande-Terre (table S2). One of them failed after a few days (RCBF0) and recorded only 2 phases. (2) Between February and November 2019, between 6 and 15 OBS were deployed and recovered every 3 to 4 months. A total of 12 INSU-IPGP short period OBS (Institut National des Sciences de l'Univers – Institut de Physique du Globe de Paris) and 48 IFREMER micrOBS or LotOBS (Institut Français de Recherche pour l'Exploitation de la Mer) were used (table S1). One instrument could not be recovered (IR3B). At present, more than 4,000 earthquakes have been manually picked and located by the MAYOBS/REVOSIMA (Réseau de Surveillance Volcanologique et Sismologique de Mayotte) seismology team. More details about instruments and earthquakes locations may be found in Saurel et al. (resubmitted) or on the REVOSIMA bulletin webpage (<https://www.ipgp.fr/fr/revosima/reseau-de-surveillance-volcanologique-sismologique-de-mayotte>). Due to the need to monitor the crisis and the lack of time or technical solution (as non-communication of the instrument), some of the instruments were not located. Their deviation due to the water current was estimated to be ~300 m. To estimate the effect of this uncertainty on the tomographic inversion, we performed two tests, presented and discussed in detail in Section 2.3.

We extracted a total of 3,843 events that occurred between February and November 2019 from the MAYOBS relocated earthquake catalog, defined as the “*initial catalog*”. The magnitude of completion is about 2.25, and the azimuthal gap mean is equal to 98° . The P and S mean number of phases are 12 and 10, respectively. The mean latitude, longitude, and depth errors are respectively equal to 1.41, 1.04, and 1.92 km, with maximum errors equal to 36.32, 53.2, and 67.5 km for the most poorly located event (figure S3). We selected a subset of the *initial catalog* based on quality criterion so that only the well-constrained events are used for the tomographic inversion: longitude, latitude, and depth errors < 5 km and a minimum of 5 P and 3 S phases recorded per station. We allowed a maximum distance to the nearest station equal or less than 30 km. These selected events have been labelled as the “*filtered catalog*”, composed of 3,699 events with 45,359 P and 39,667 S phases.

2.2. Inversion Method and Parameters

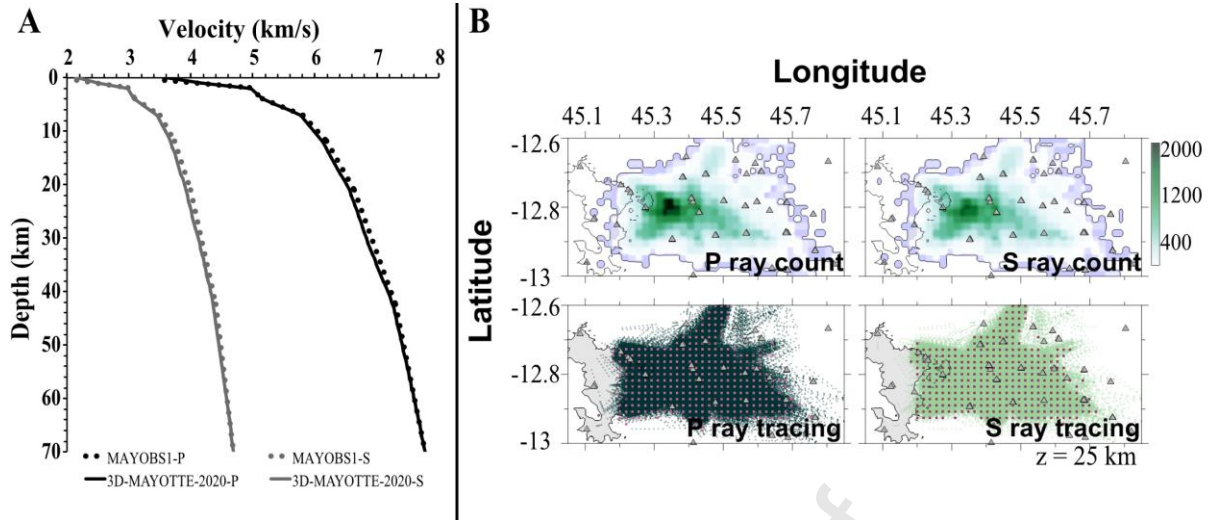
To calculate the 3D seismic velocity variations in the Mayotte region, we used LOTOS (Koulakov, 2009). LOTOS jointly inverts for P and S velocity structures, source coordinates, origin times, and station corrections through the LSQR method (Paige & Saunders, 1982). First, the algorithm optimizes an input 1D velocity model, through 2-4 iterations, and calculates new source locations in the model. The algorithm may generate preliminary source locations, if they do not exist. The source locations in 1D are based on a goal function (GF), reflecting the probability of a source to be located at a current point (Koulakov & Sobolev, 2006). The ray travel times are corrected for station elevations. The GF probability is performed by a grid search method. Second, the optimized 1D velocity model and source locations are then used as initial conditions for a 3D velocity inversion. Sources are relocated with a 3D ray tracing (or bending) method based on the Fermat principle of travel time minimization. The preferred locations are chosen using the GF and a gradient method (Koulakov et al., 2006).

LOTOS 3D inversion is performed through 3-5 iterations, on four grids with azimuthal orientations of 0, 22, 45 and 66 degrees to avoid artifacts related to node distribution (figures S4 and S5). This orientation is given from the center of the model (45.44, -12.8) where each node will undergo a clockwise rotation in latitude and longitude coordinates. Each grid is based on a mesh of nodes fixed in a volume on vertical lines. A uniform spacing distribution is used in map view. On vertical lines, nodes are distributed according to the ray occurrence, such that if there is no ray, then there is no node (figures 2 and S6). Nodes will then be mostly near stations but also at any depth and distance between the source and receiver where the ray travels. Between nodes, velocity values are linearly approximated. The output model, at each iteration, is the average differential of velocity (ΔV) between the optimized input 1D velocity model and the 3D output. The chosen inversion parameters are described in table 1.

The LOTOS inversion is performed through the LSQR method (Paige & Saunders, 1982). This method is used in 1D for the inversion of the sparse matrix composed of the free parameters (weights in table 1) and in 3D for the inversion of the first derivative matrix (Koulikov, 2009). In other words, LSQR iterations are specifically related to the minimization between the starting model and the final model. It is one step of the inversion that is performed within the upper 3-5 iterations of the overall inversion. The larger the value, the sharper the solution is. We chose a high value to ensure the convergence of the process (LSQR ite= 80). Weight on P and S velocity models are needed for the inversion process (Vp wgt / Vs wgt). We used equal phase weights in this study. In the joint inversion process, the velocity and hypocenter partial derivative matrix is supplemented by two sub-matrices that influence the velocity perturbations: a smoothing and a regularization matrix. Increasing the weight on smoothing (P smth / S smth), induces a decreasing effect on the anomaly differences in neighboring nodes. From the regularization parameter, increasing its weight (P reg / S reg) reduces the inverted Vp and Vs anomaly amplitudes. Hypocentral shift (Hor wgt / Ver wgt)

and origin time (Time wgt) weights are also required. These parameters relatively control hypocentral and velocity perturbations. We choose values based on Koulakov (2009). Finally, the software allows for station corrections (P st. wgt / S st. wgt). As our study aims to map travel time variation, we kept a very small weight on this value. In the end, we tested inversion parameters one by one by evaluating their effect on checkerboard and RMS time residuals. The parameter value that gave the best solution regarding checkerboard and RMS time residuals was chosen before running tests with another inversion parameter. In total, we performed 92 model tests and examined them to determine our optimal model parameters.

For our analysis, we use the velocity model developed during the MAYOBS1 oceanographic cruise, named MAYOBS1 (Saurel et al., resubmitted). We used locations from the *filtered catalog*, and seismic station locations. Our P and S velocity models are respectively composed of ~16,800 and ~16,600 nodes over a $110 \times 90 \times 70 \text{ km}^3$ (x, y, z) velocity grid volume with 2 km of node spacing in horizontal (table 1 and figure 2). We calculated the P and S models roughness as the integrated square of the second differences of the velocity model in 3D (Lees & Crosson, 1989; Zelt & Barton, 1998). RMS time residuals and roughness per iteration give us an optimal solution after three iterations (figure 3), where the RMS was not significantly decreasing and roughness continued to increase. After three iterations in the 3D inversion, the P and S residuals average has been reduced from 0.17 s and 0.27 s to 0.12 s and 0.17 s (29.41% and 37.03% of reduction). The mean earthquake locations uncertainty for this iteration is 3.17 km.



LOTOS parameters for the joint inversion

Name	Value	Description
LSQR ite	80	Number of LSQR iterations, the larger value, the sharper solution is
Vp wgt / Vs wgt	1/1	Weights P and S velocity parameters
P sth / S sth hor.	0.4/0.5	Smoothing level applied in horizontal and vertical directions. The larger value of these parameters, the smoother models become
P sth / S sth ver.	0.2/0.4	
P reg. / S reg.	0.8/1.4	Damping level applied. Increasing these parameters induces the decrease of anomaly amplitudes
P st. wgt / S st. wgt	0.0001/0.0001	Station correction weights for P and S data
Hor. wgt / Ver. wgt	5/5	Horizontal and vertical weight applied on source shift
Time wgt	1	Weight applied on time shift

Table 1. LOTOS inversion parameters. Descriptions and values of the parameters used for the inversion. Ite: Iterations. Wgt: Weight. Hor.: Horizontal. Ver.: Vertical. Reg.: Regularization. St.: Station.

Fig. 2. Models and ray input overview. A: the dotted lines represent the initial 1D velocity input models (MAYOBS1) and the solid lines are the average velocity of the 3D velocity model outputs at iteration 3 (3D-MAYOTTE-2020). B: example of horizontal cross sections at 25 km depth for P and S ray count, tracing (dark and light green dots) and node distributions (pink dots) in a 0° grid orientation. Section thickness for nodes and rays visualization is equal to 1 km each side. Grey triangles mark land and offshore seismic station locations.

[COLOR NEEDED]

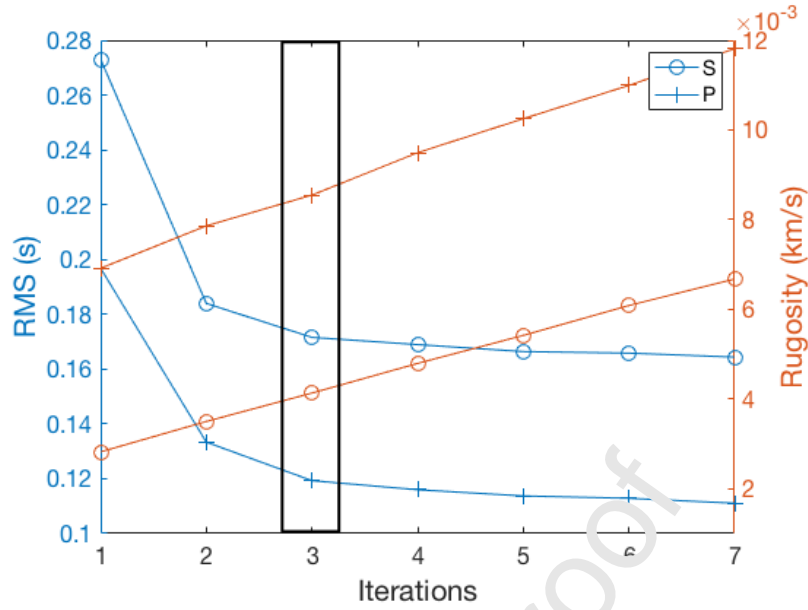


Fig. 3. P and S RMS time residual and roughness per iteration for the 3D output velocity model. The black rectangle indicates the chosen iterations.

2.3. Synthetic tests

To assess the capacity of our dataset to solve the geometry and amplitude of velocity anomalies, we conducted horizontal and vertical checkerboard tests, free-shape anomaly tests, and ray coverage and count analysis (table 2). Synthetic tests travel times were computed between source-receiver pairs as in the real observation system. They are then perturbed by random noise with an average standard deviation of 0.1 s for P and 0.2 s for S, corresponding to P and S manual mean of pick time residuals (figure S7). Checkerboard test size was varied from 5x5x100 to 15x15x100 km in horizontal map view and from 5x100x5 to 15x100x15 km³ with $\pm 10\%$ of velocity variations for vertical cross-sections. Free-shape anomaly form tests have been determined on the basis of observed patterns resulting from the real data inversion. The latter are set using polygonal forms within defined spatial location and velocity

anomaly values. Velocity anomalies vary from $\pm 1\%$ to $\pm 7\%$. For further understanding of our models limitations, we conducted 3 supplementary synthetic tests. Test 1 demonstrates how isolated structures may be recovered. For test 1, we used another checkerboard test with a 10 km^3 size and with $\pm 10\%$ velocity variation. Test 2 demonstrates the capacity of our model to retrieve horizontally elongated anomalies as sills. For test 2, we conducted $120 \times 40 \times 10$ km rectangles along the -12.8° direction and $70 \times 60 \times 10$ km rectangles along the 130°N direction and inverted with the same velocity variations. Test 3 is another free-shape anomaly forms test, with a Smiley shape as proposed by Koulakov (2009). In test 3, we used $\pm 6\%$ of velocity variation.

To assess the uniqueness of our velocity anomalies, we changed the 1D velocity model input in LOTOS inversion, and kept original earthquake locations and inversion parameters similar. We compared here three different models (figure S8):

- “MAYOBS1”: previously described and corresponding to the chosen input velocity model.
- “AK-135”: spherical Earth average velocity model name AK135-F and determined by Kennett et al., (1995), which is a neutral model for Mayotte region.
- “Alav_simplified”: a simplified version of the 1D velocity model developed by Lavayssière et al., (2020) using VELEST. The 1D velocity model was developed using 813 best constrained events from February to November 2019 from the same *initial catalog* in this study. Lavayssière et al. (2020) used the 1D ADofal model as input. The latter is based on a S-wave velocity profile calculated from receiver functions on the Mayotte Island (Dofal et al., 2018).

Elongated rectangles from $5 \times 5 \times 100$ to $15 \times 15 \times 100$ km size and from $5 \times 100 \times 5$ to $15 \times 100 \times 15$ km checkerboard and free-shape anomaly tests indicate a good resolution beneath the network with a minimum anomaly size of 5 km into the PSC (figures 4 to 6 and S9 to S12). The 10 km^3 also highlight a good recovery between 10 km and 40 km depth despite the

velocity variations with depth (figure S13). This is supported by a good ray coverage and count in the PSC area due to the very active seismicity (figures 2, S14 to S16). The best anomaly shape recovery is obtained with a dimension of 10 km. Anomalies of 15 km is the upper limit of synthetic anomaly size because of our ray coverage, but it is still quite well-resolved. Synthetic anomalies cannot be solved below 40 km depth. Our ray coverage does not allow us to resolve velocity variations below the NVE. From the change of 1D input velocity model test, main velocity anomalies are still present as the high P velocity anomaly ($\sim +3.5\%$) and low S velocity anomaly ($\sim -5\%$) at 25 km depth around the PSC (figure S17). All the anomalies exposed in this study are presented regardless of these parameters.

On another hand, elongated rectangles of $120 \times 40 \times 10$ km along the latitude -12.8° and of $70 \times 60 \times 10$ km along the 130°N direction could not be well resolved (figure S18). Only the anomaly around 30 km depth, where the PSC is located, could be retrieved in both P and S models. This indicates that our model is unable to image elongated horizontal layers as sills, even if they exist.

LOTOS parameters for synthetic tests

Model Name	Anomaly size (km)	P/S noise (s)	Amplitude of anomalies
<i>Horizontal checkerboard tests</i>			
CBHOR_05	5x5x100	0.1/0.2	±10%
CBHOR_10	10x10x100	0.1/0.2	±10%
CBHOR_15	15x15x100	0.1/0.2	±10%
<i>Vertical checkerboard tests</i>			
CBVER_05	5x100x5	0.1/0.2	±10%
CBVER_10	10x100x10	0.1/0.2	±10%
CBVER_15	15x100x15	0.1/0.2	±10%
<i>Free shape anomaly tests</i>			
SYNTHOR1	Manually digitized	0.1/0.2	Vary from ±1 to ±7%
SYNTVER1	Manually digitized	0.1/0.2	Vary from ±1 to ±7%
SYNTVER2	Manually digitized	0.1/0.2	Vary from ±1 to ±7%
SYNTVER3	Manually digitized	0.1/0.2	Vary from ±1 to ±7%

1.

Table 2. LOTOS parameters for the main synthetic test inversions. Descriptions and values of the parameters used for the inversion of synthetic tests. Free shape anomalies were manually digitized from the Vs 3D output model. Each anomaly has a given amplitude value, according to the 3D output model, and varies from ±1% to ±7%.

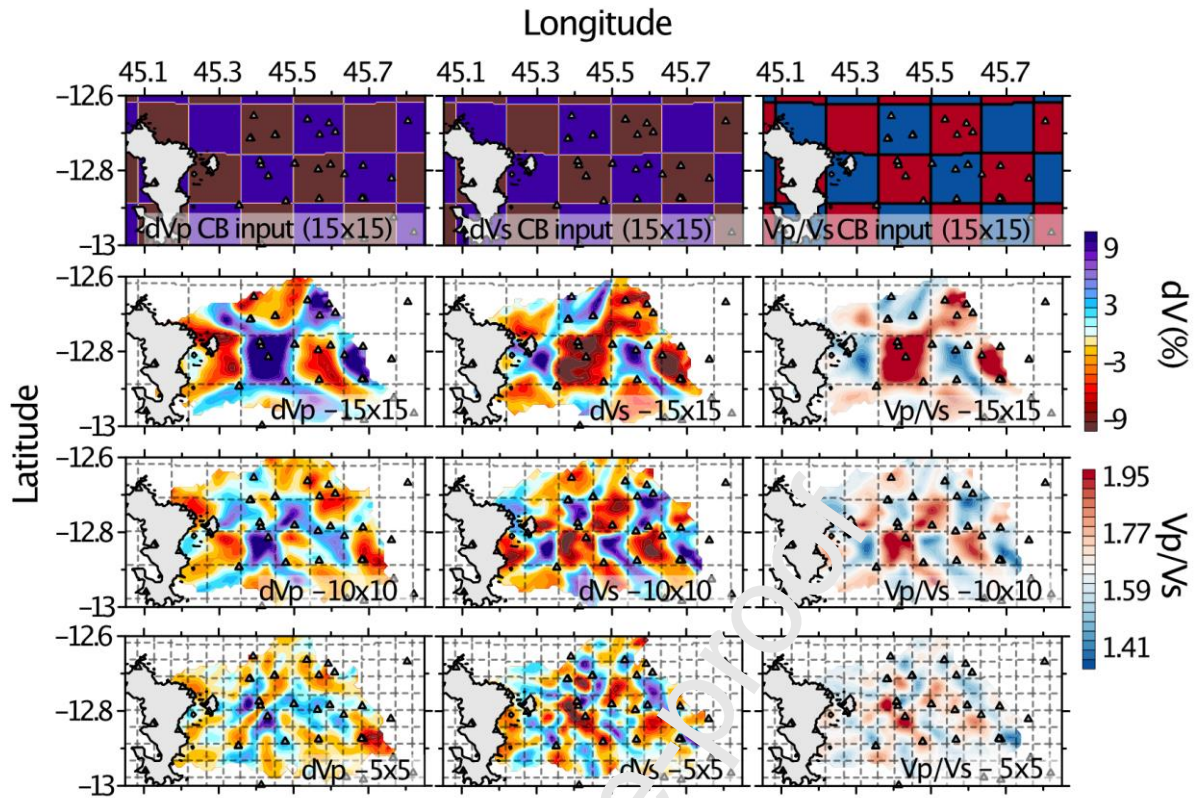


Fig. 4. Horizontal checkerboard tests. Examples at 25 km depth of checkerboard tests for dVp (left), dVs (center) and Vp/Vs (right). At the top are 3 examples of input. The 3 following lines are output for 15x15, 10x10 and 5x5 km² square size, respectively. Small triangle: seismometers. Black square: NVE, New Volcanic Edifice. Dashed lines: contour line of the input checkerboard. The white masked area delineates where there are no rays with a distance to the nearest node equal to 2 km. [COLOR NEEDED]

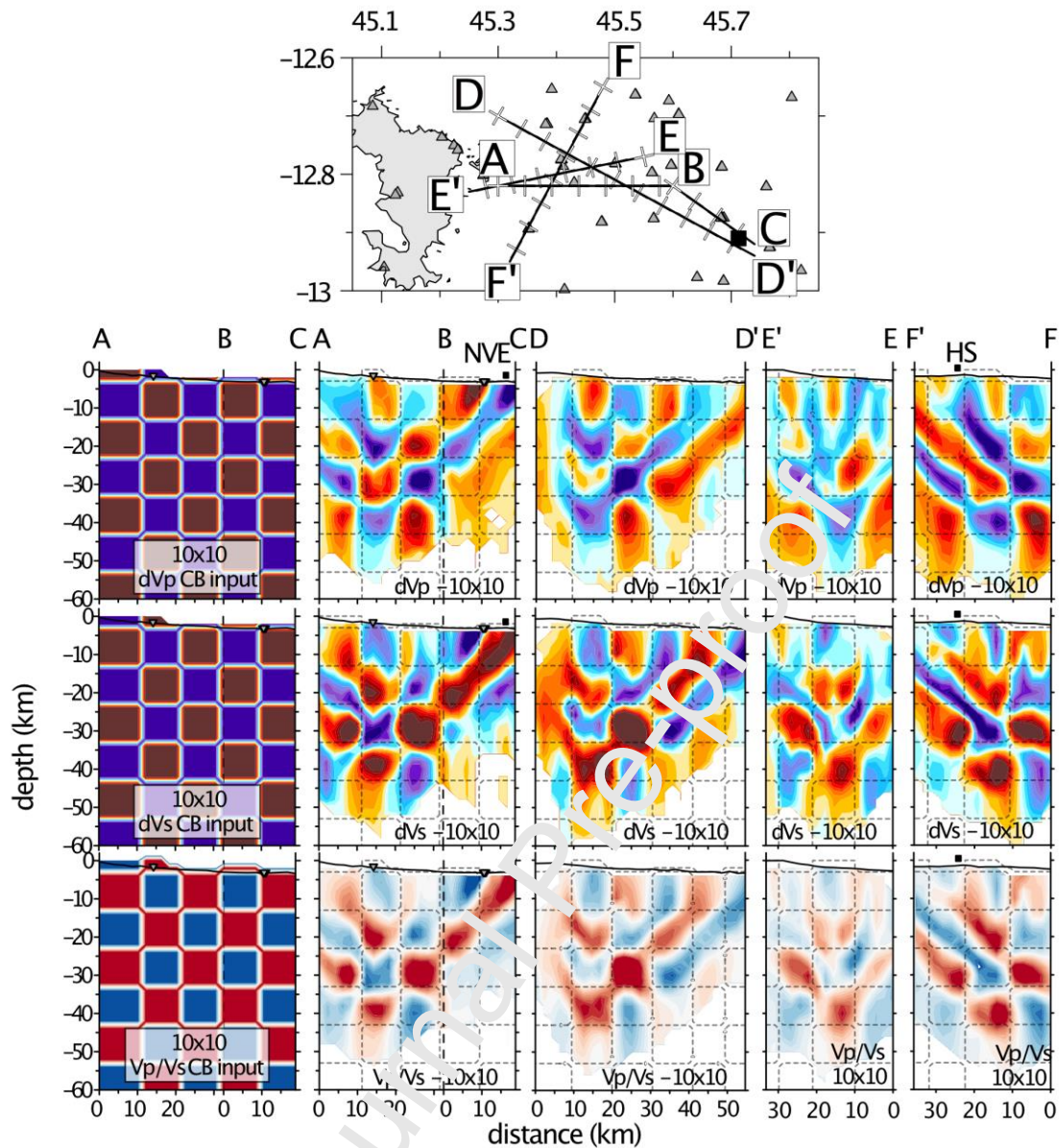


Fig. 5. Vertical checkerboard tests. Examples of vertical checkerboard tests for $10 \times 10 \text{ km}^2$ square size. The 4 cross-sections are indicated at the top on the map view. Triangles are seismometers. Left column is an example of input for the ABC cross-section. The following 4 columns are output for the 4 cross-sections. Top line: dVp. Center line: dVs. Bottom line: Vp/Vs. Color scales are the same as in figure 4. NVE: New volcanic edifice. HS: Horse Shoe. Triangles and dashed lines are explained in figure 4. The white masked area delineates where there are no rays with a distance to the nearest node equal to 2 km. [COLOR NEEDED]

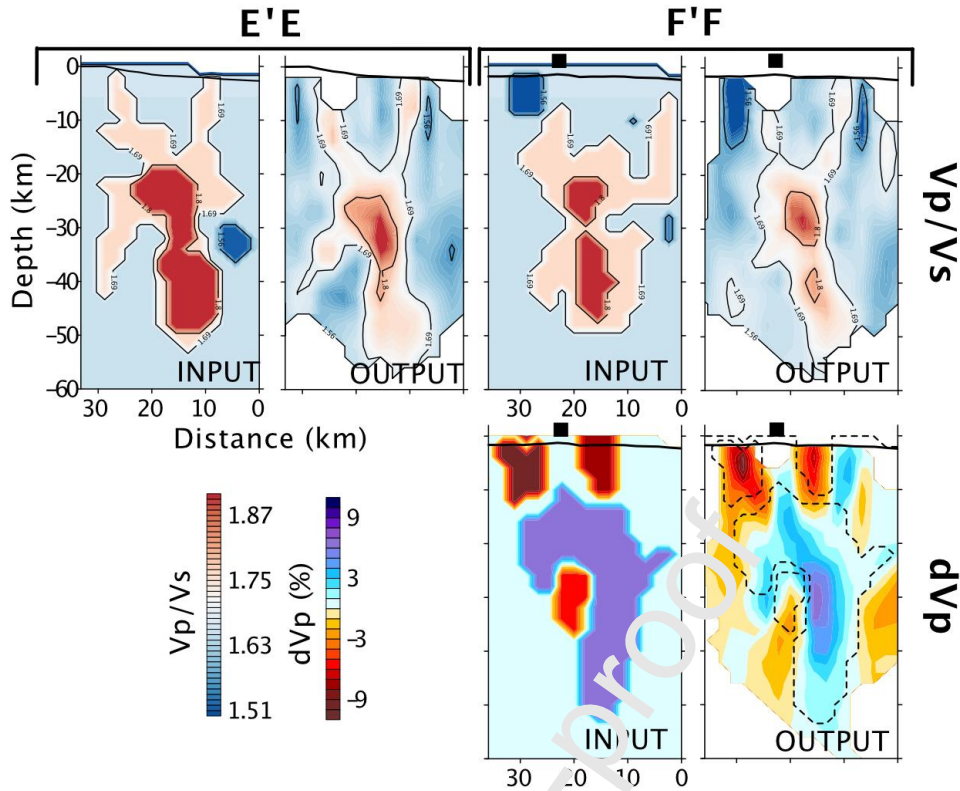


Fig. 6. Free-shaped anomaly tests. Vertical cross-sections, examples of free-shaped anomaly tests for EE' and FF' cross-sections. The two cross-sections are located on the map view on figure 5. INPUT: Input anomalies. OUTPUT: Output after the inversion at iteration 3. Dashed lines on OUTPUT dVp highlight INPUT contours. Black square: *Horse Shoe* position. The white masked area delineates where there are no rays with a distance to the nearest node equal to 2 km. [COLOR NEEDED]

To estimate the effect of OBS location uncertainty on the tomographic inversion, we performed two tests, where we randomly moved the OBS positions by adding 212 or 424 m on the azimuthal plane (figure S19, S20). We found that the anomaly shapes were not strongly influenced and that only a small change in the amplitude occurred. The estimated effect on the dVp and dVs models on 4 horizontal cross sections at 10, 15, 25 and 35 km depth is $\sim 0.25 \pm 5.78\%$ (dVp) and $\sim 0.50 \pm 9.03\%$ (dVs) for a 212-m mislocated OBS (figure S19) and $\sim 0.35 \pm 6.71\%$ (dVp) and $\sim 0.65 \pm 10.08\%$ (dVs) for 424 m (figure S20). Large uncertainty values are only present at the edge of the models, mainly around the NVE area, where there are not enough rays crossing. The models are therefore not strongly affected by the uncertainty of

OBS locations and do not prevent us from interpreting our final tomographic inversion. However, this uncertainty has to be taken into consideration if another passive tomography is calculated in the same area, with the aim of exploring the evolution with time of the volcanic plumbing. As the seismic network will be different, the velocity variations between this tomography and the new calculated one have to be higher than the latter calculated uncertainties.

3. Results

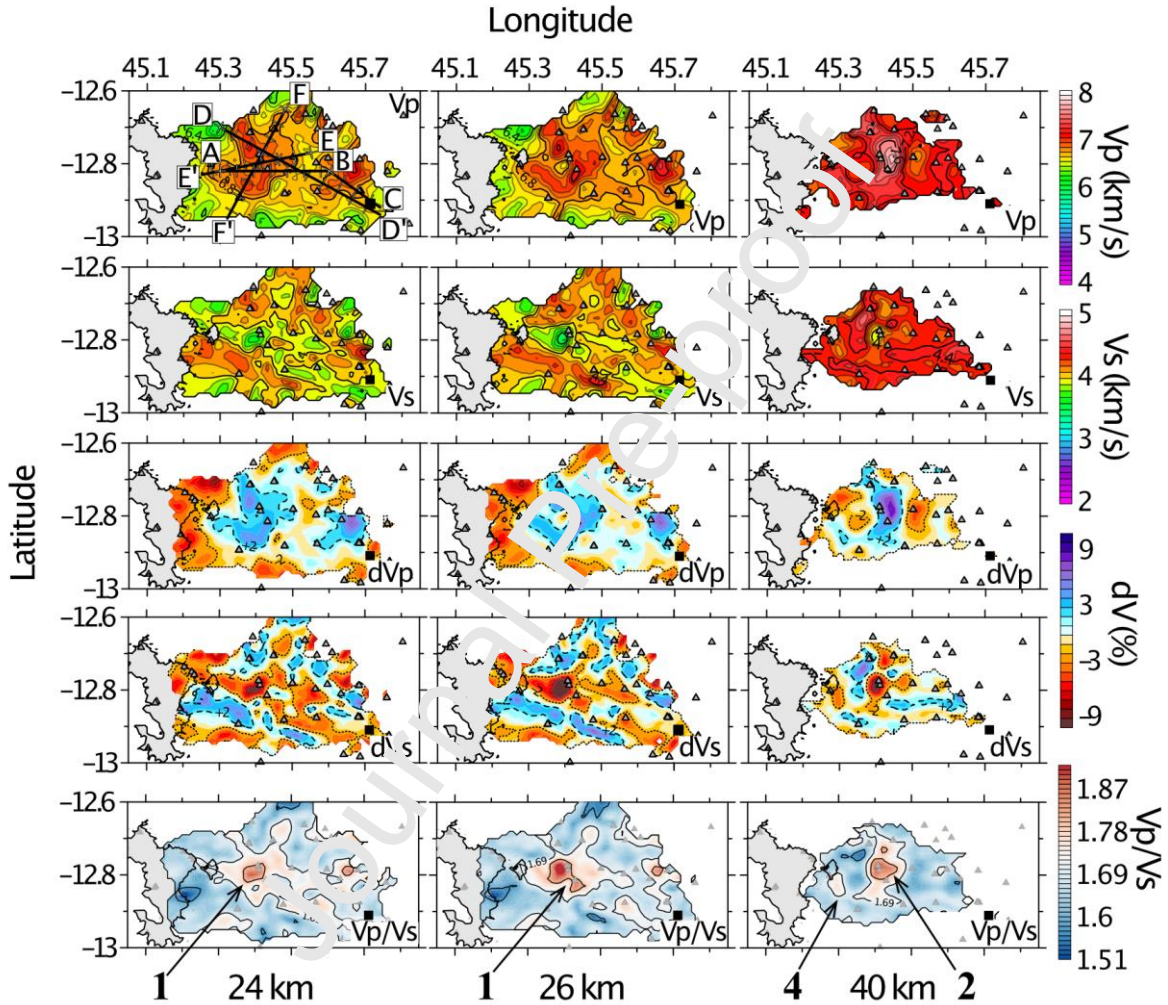
3.1. Velocity models

Figures 7 and 8 illustrate our 3D velocity models (V_p , dV_p , V_s , dV_s and V_p/V_s) in horizontal and vertical cross-sections, respectively. Notable anomalies are labeled from 1 to 6, as indicated on V_p/V_s cross-sections or maps, do not surcharge the figure, even if they are present in the other models. Some supplementary cross-sections of dV_p and dV_s models may be found in figures S21 to S24, as well as a video (video V1) of the V_p/V_s model.

In general, besides the highlighted structures we call « velocity anomalies » in this study, the overall V_p and V_s model present really low velocity in the crust and in the mantle. Taking a Moho at 17 km (Lisfi et al., 2018), the mean V_p in the crust is equal to 5.6 km/s and V_s to 3.3 km/s, which is lower than typical values for oceanic crust (6.5-7 km/s for P and 4 km/s for S). For deep depths, for example at 30 km depth (figures 1-A and 7), V_p is lower than 8 km/s and V_s lower than 4.4 km/s, which are typical values for uppermost mantle. The approximate mean V_p is about 6.8 km/s and V_s is about 4.1 km/s. What we will later refer to « fast » and « low » velocity anomalies are relative to these observations. We cannot exclude that the first 10 km are less resolved because of ray crossing geometry (figure S15 and S16) and are therefore more influenced by the input velocity model.

A first striking anomaly is observed between depths of 20 and 35 km, below the *Horse*

Shoe (HS), in the PSC area (figures 7-8, labeled 1). Its diameter varies from 7 to 12 km, and it can be imaged by our inversion. Anomaly 1 is characterized by low V_p (< 6.8 km/s), low V_s (< 3.9 km/s), low dV_p ($> -3\%$) and low dV_s ($> -4\%$). The V_p/V_s ratio ranges from 1.8 to a maximum value of 1.92 in its center. Considering an isosurface of V_p/V_s ratio equal to 1.8



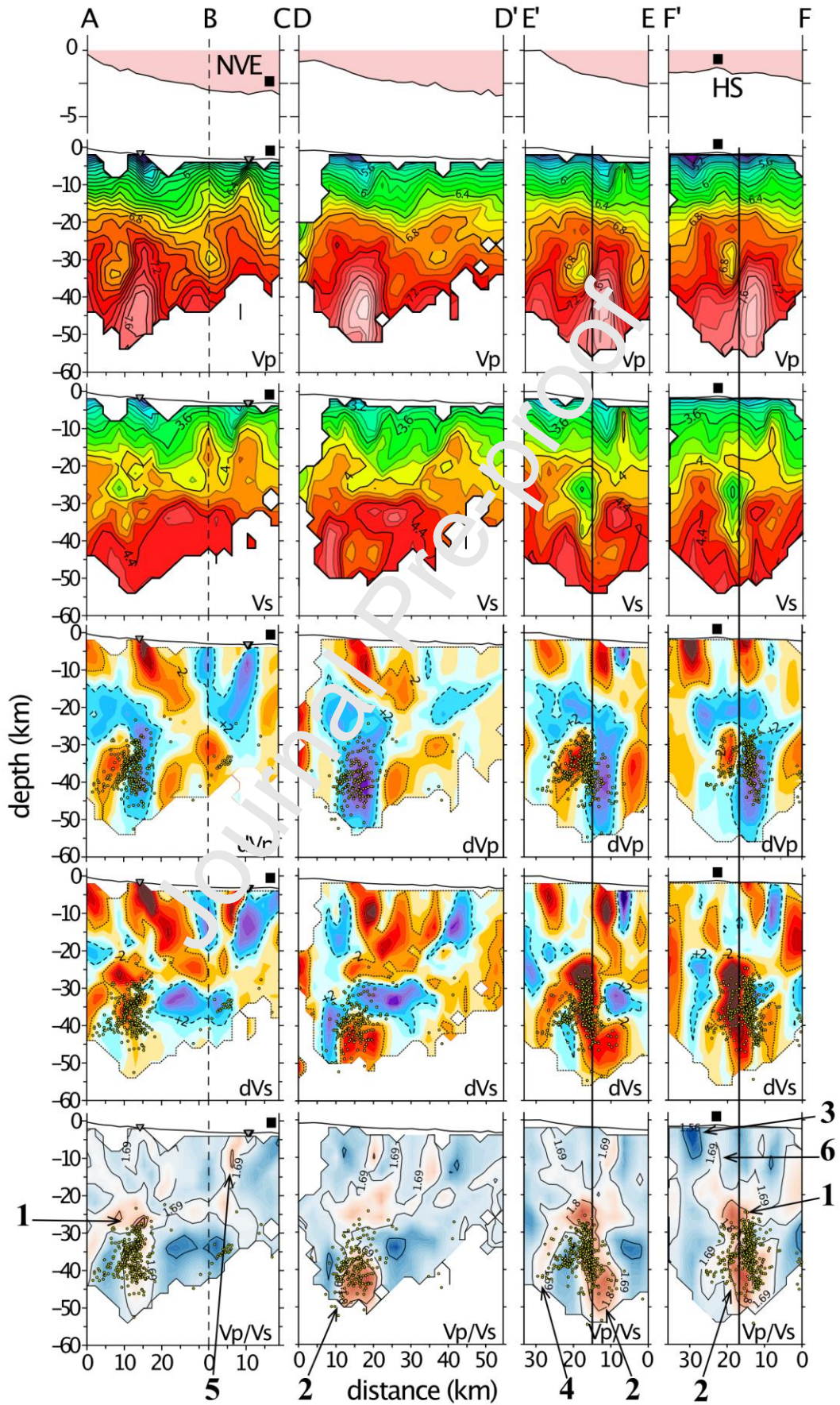
using Voxler (Golden Software), we obtained a volume of this body equal to 205 km^3 .

Fig. 7. Horizontal cross-sections of the output velocity models. Horizontal cross-section at 24 (left column), 26 (center column) and 40 (right column) km depth for V_p , V_s (top lines); dV_p , dV_s (center lines) and V_p/V_s (bottom line). Mayotte islands are represented in light grey. Triangles are seismometers used for the study. Vertical cross-section illustrated on figure 8 are located on the top-left map and on figure 5. The black square marks the location of the NVE. The white background masks indicate the area where there are no rays. V_p , V_s : solid black lines are isovelocity contours every 0.4 km/s; solid light lines are isovelocity contours every 0.1 km/s.

dVp, dVs: black dashed lines are the +2% isocontours; block dotted lines are the -2% isocontours. Vp/Vs: solid black lines indicate two isocontours: 1.68 and 1.8. The large black numbers (1, 2 and 4) indicate anomalies described in Section 3. **[COLOR NEEDED]**

Journal Pre-proof

Fig. 8. Vertical cross-sections of the output velocity models. Symbols and notations are the same as in figure



7. From top to bottom: A bathymetry exaggeration, V_p and V_s , dV_p and dV_s , and V_p/V_s images. Yellow dots on dV_p , dV_s and V_p/V_s cross-sections are earthquake locations on a slice of 1 km (0.5 km each side). Traces of the cross-sections and color scales are shown in the figure 7. The black squares indicate the position of the NVE (New volcanic edifice) and the HS (Horse Shoe) bathymetric feature. The black dashed vertical line on the ABC cross-section indicates the position of the change in the section orientation. The black vertical solid lines on EE' and FF' cross-sections are a visual support to easily observe the limit between the anomalies 1 and 2. [COLOR NEEDED]

A second notable elongated anomaly is observed between depths of 35 and 50 km, in the same region, slightly East of anomaly 1, in the PSC area (figures 7-8, labeled 2). Its width and length vary from 8 to 17 km. The anomaly can be imaged, but our inversion cannot recover well velocity variations below ~43 km depth, making any interpretation below that depth as speculative. Only the top of this anomaly is recovered by our free-shape anomaly tests (figure 6). Anomaly 2 is characterized by high V_p (>7.2 km/s), heterogeneous V_s , high dV_p ($> +2\%$) and heterogeneous dV_s ($> +2\%$ around 30-35 km depth and $< -2\%$ around 40-50 km). The V_p/V_s ratio varies from 1.65 to more than 1.8 in the lower and eastern part. Considering a V_p/V_s ratio isosurface of 1.8, the volume of anomaly 2's body is equal to 234 km^3 , but this volume could be over or underestimated as we do not have resolution below 43 km depth.

A third feature is observed on the cross-section FF', between 0 and 10 km depth, South of the HS, 25 km away from Petite-Terre (figure 8, labeled 3). Its width and length is equal to $5 \times 5 \text{ km}^2$, in a region where an anomaly of this size is at the limit of resolution (figure S11). A free-shaped anomaly test (figure 6, FF', blue high V_p/V_s ratio and red low dV_p at 30 km of distance) indicates that this anomaly could be resolved but appears a bit bigger than in reality. Anomaly 3 is characterized by very low V_p (~ 4.8 km/s), no apparent change in the V_s model, very low dV_p ($< -8\%$), and no apparent change in dV_s . The V_p/V_s ratio is about 1.50-1.56, with a minimum of 1.44 into the center. Considering a V_p/V_s isosurface equal to 1.56,

anomaly 3's body volume is equal to 42 km^3 , but this volume is likely overestimated as our free-shape anomaly test indicates.

Anomaly 4 is a nearly vertical branch just below Petite-Terre that extends from anomaly 1 (cross-section EE', figure 8). This nearly vertical branch is located between 30 to ~ 47 km in depth. Its width is about 8 km, and according to a free-shaped anomaly test this branch is resolvable (figure 6 and S25). Anomaly 4 is characterized by a small decrease in V_p and V_s , illustrated by a U-shape in the isovelocity contours (figure 8). In the dVp model, we cannot distinguish anomaly 1 from 4; they seem to be connected. In the dVs model, we can clearly observe a branch from anomaly 1 with decreasing dVs (from -2 to -4%). Anomaly 4 has a V_p/V_s ratio of about 1.72.

The 5th notable anomaly is located between 3 and 15 km depth, West of the NVE and seemingly "pointing" in the direction of the NVE (cross-section BC, figure 8). Its width and length are about 5 km, in a region where this anomaly size could be solved (figure S11). Anomaly 5 is characterized by a slight decrease in V_p and V_s . The dVp model does not give relevant velocity variation. The dVs model is characterized by a very low velocity anomaly ($< -4\%$). The V_p/V_s ratio is higher than 1.8 in this region. More to the East, below the NVE, the resolution is not sufficient to determine any remarkable anomaly. Considering an isosurface equal to 1.8, we obtained a volume for this anomaly body to be equal to 94 km^3 .

Anomaly 6 has a vertical elongated shape and extend from the top of the anomaly 1 to the subsurface, below the HS relief (cross-section FF', figure 8). Its length is about 9 km, making it resolvable (figure 6). Anomaly 6 is characterized by slight increase in V_p , and a slight decrease in V_s . The dVp model doesn't give relevant velocity variation. In the dVs model, the anomaly has an amplitude equal to +2.5%. The V_p/V_s is slightly higher than 1.71.

Finally, taking an isocontour V_p/V_s ratio equal to 1.69, we observed several branches that connect the different anomalies (1, 2, 4, 5 and 6) to each other (V_p/V_s ratio on figure 8).

Anomaly 1, appears to be a central anomaly with several branches emerging both up and down, reaching the surface and connecting to seafloor reliefs (cross-sections DD' and FF', figure 8), and going East, toward the NVE (cross-section ABC, figure 8). In horizontal cross-sections (24-26 km depth, figure 7), the branches have a N130° orientation in the dVs and Vp/Vs models, parallel to the volcanic ridge. However, the dVp model does not provide any relevant velocity variations. To exclude the possibility of an artifact, we conducted three different tests. First, we inverted our data into the four grid orientation (Section 2.3) proposed by LOTOS to evaluate the influence of the nodes on the N130° anomaly (0°, 22°, 45° and 66°). Regardless of the grid we used, the anomaly persists (figure S5). Next, we explored the influence of the 1D velocity input (Section 2.3). No matter the 1D input model, the N130° anomaly still exists (figure S8). Finally, we inverted a free-shape anomaly test based on the later anomaly shape to be sure that our data may recover it. The output velocity from this test indicates that the N130° anomaly is recovered quite well (figure S26).

3.2. Seismicity distribution

Figure 8 displays earthquake locations obtained after the inversion. Their average displacement in longitude, latitude, and depth from the *filtered catalog* at iteration 3 are respectively equal to 1.43, 1.00 and 1.27 km. Seismicity is primarily concentrated in PSC, which is an elongated cluster in the vertical direction, between 25 and 55 km depth. This seismicity delineates dVp positive and negative amplitudes between anomalies 1 and 2 (sections ABC, EE', and FF', figure 8). In the dVs model, it is difficult to associate the seismicity distribution to velocity changes, except along section FF' where the earthquakes are well aligned South of the negative anomaly. On the Vp/Vs sections, the PSC is well associated with the South and West border of the 1.8 Vp/Vs isocontour. In section BC, several events associated with DSC form a dipping alignment pointing toward the NVE.

4. Discussion

From our 3D velocity models, we propose to interpret the velocity anomalies as possible multiple magmatic reservoirs between the mantle and crust, and we discuss the old plumbing system between these reservoirs, the occurrence of gases, and the role of the inheritances.

4.1. Low velocity crust and mantle

Low P and S velocities characterizing the crust could be explained either by the presence of gas (HS has observable degassing), the presence of multiple fractures and cracks due to regional strain (Feuillet et al., 2021; Famin et al., 2020), or by the basaltic composition of the crust (Berthod et al., 2021). Unfortunately, the first 10 km are less resolved because of ray crossing geometry. Further study is in process to learn more about the crust through active seismic imagery (Sismaore marine cruise, Thinon et al., 2020). At slightly deeper depths, the Moho has been determined to be at 11 km (Dofal et al., 2018). From our study, the velocities below 30 km depth are about 6.8 km/s for the V_p and highly perturbed. Moreover, the overall area seems to have very low V_p and V_s . Darnet et al. (2020) conducted a magnetotelluric (MT) survey through Petite-Terre and the PSC. The MT survey indicated the presence of a drop (two orders of magnitude) in the rock resistivity at about 15 km depth. Changes in rock resistivity can be influenced by hydrothermal and/or magmatic fluids. Darnet et al. (2020) interpreted this resistivity drop as possibly due to partial melting. As discussed by Feuillet et al. (2021), the lithosphere-asthenosphere boundary in place between Mayotte and Madagascar is composed of a high-velocity lithosphere and a low-velocity asthenosphere. Barruol et al. (2019) interpreted the low-velocity asthenosphere as hot material spreading beneath and beyond the Mascarene basin. Hot oceanic lithosphere base combined with a damaged mantle

and crust, induced by regional rifting, may favor large volumes of melts (Feuillet et al., 2021). The latter hypothesis may be illustrated in our study by these low P and S velocities, suggesting for a widespread melt throughout the region.

Our interpretations of Mayotte's volcanic system mainly benefit from Lees (2007), which gives an overview of seismic tomography of magmatic systems. Fractured rocks, the lithological nature of rocks, the presence of water, oil, gas, or magmatic fluids, and anisotropy may have an influence on the V_p/V_s ratio. Comparing V_p/V_s ratio with V_p (or dV_p) and V_s (or dV_s) values and geological information of the area is crucial for interpreting tomography results. Using Mayotte stations (local) and Glorieuse and Karthala stations (regional) gave a local and regional V_p/V_s ratio mean determined from MAYOBS data to be 1.66 and 1.72, respectively (Lavayssière et al., 2020; Saurel et al., *resubmitted*). These V_p/V_s ratios fall between 1.5 and 2, which are generally accepted for more consolidated rock materials. Lavayssière et al., (2020) highlight a 7 km layer with a ~ 1.8 V_p/V_s ratio indicative of the magmatic nature of the crust, upon a ~ 1.6 V_p/V_s ratio below 10 km that they interpret as influenced by faulting and/or the presence of fluids. While, sandstones can have V_p/V_s ratios varying from 1.66 to 1.81 and carbonates from 1.81 to 1.98 (e.g. Hamada 2004), the nature of the Comoros basin remains unclear (Phethean, 2016). Therefore, it is difficult to make a direct comparison of our V_p/V_s values with oceanic or continental crust V_p/V_s values. Based on the works cited above, and because our results are mainly concentrated below 10 km depth, we consider everything higher or lower than the V_p/V_s local mean (1.66) as an anomaly.

4.2. Multiple reservoirs

Anomaly 1 (~ 28 km depth beneath HS), defined by low dV_p and dV_s and high V_p/V_s ratio (more than 1.8) could be characteristic of the presence of mush and partial melt (e.g. Nakajima et al. 2001; Lees 2007). This combination of low V_p and high V_p/V_s ratio may also reflect a strongly fractured body filled with fluids (Bazin et al., 2010). After dredging the HS

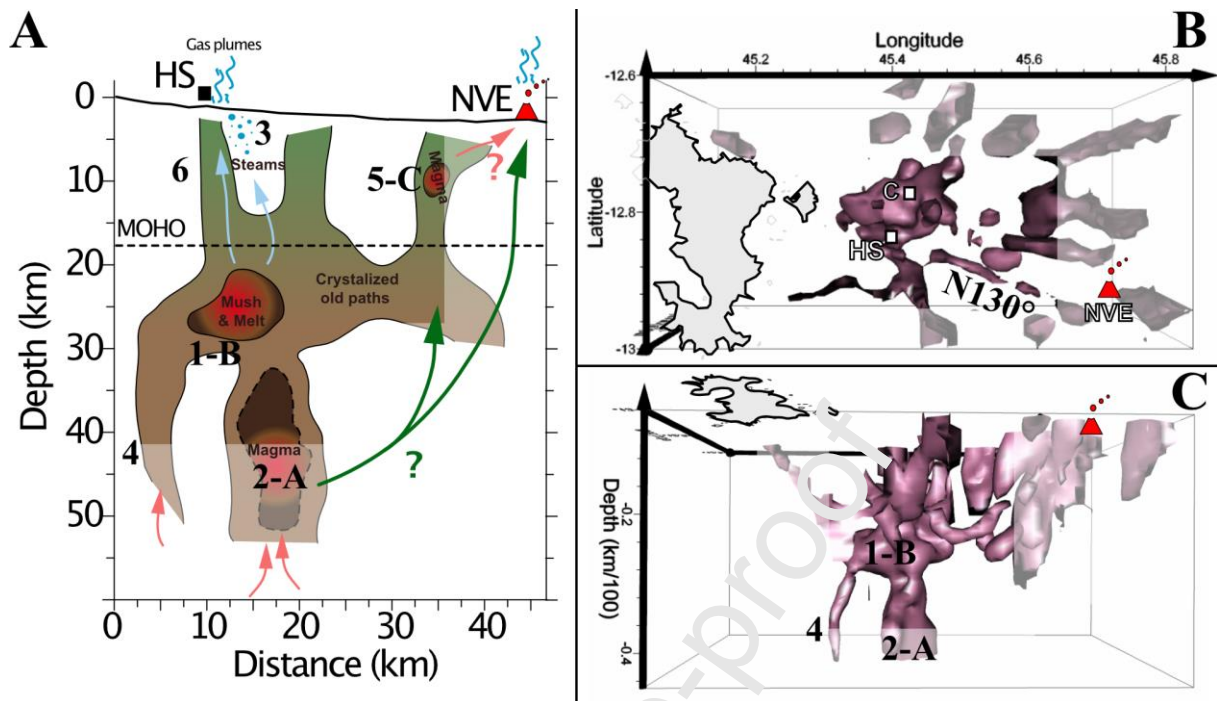
region, Berthod et al. (in press) conducted a geobarometry analysis on two xenoliths pyroxenes. They identified the presence of a shallow reservoir, located just below the crust and mantle boundary, storing phonolitic magma. We can make the hypothesis that anomaly 1 could be an evolved reservoir, corresponding to the Berthod et al. (in press) phonolitic reservoir, responsible to the HS volcanism. The VLF seismic activity has been located in the same area (Laurent et al., 2020), where Feuillet et al. (2021) proposed the existence of a reservoir. We rename it as reservoir B (Figure 9).

The depth of anomaly 1 is in agreement with GNSS modeling of Lemoine et al. (2020) that determined the presence of a reservoir at 28 km depth, and Cesca et al. (2020), at 30 ± 5 km. Through VLFs modeling, the latter authors determined a reservoir diameter of about 12 km and 10 to 15 km respectively. This is consistent with our findings, as we determined the diameter of anomaly 1 varying from 7 to 12 km. However, they both located the reservoir further East, at about 30 km from the coast (i.e., Lemoine et al., 2020), whereas Feuillet et al. (2021) determined a deflation source at 40 km far from the coast and at 40 km depth. Because of poor azimuthal coverage, longitude is less constrained. Taking into account the combined errors on GNSS modeling and tomography inversion, anomaly 1 and the reservoir identified by Lemoine et al. (2020) and Cesca et al. (2020) could be the same or distinct body. Indeed, the GNSS modeling demonstrated an overall deformation and could not distinguish if several reservoirs are involved. The GNSS inversion could be a combined result of anomaly 2 and a reservoir below the NVE effects. We cannot exclude the possibility of a reservoir at 30-40 km far from the coast that we are unable to image in this study due to ray coverage.

Anomaly 2 (~44 km depth) is defined by high V_p , low V_s , and high V_p/V_s ratio (larger than 1.8) which seems to be an indicator of liquid phase, volatiles, or melts (De Natale et al., 2004; Vargas et al., 2017; Kuznetsov et al., 2017). In volcano tomography studies, this could represent a magma reservoir with more primitive composition of mafic magmatic cu-

mulates, saturated with volatiles that may carry a gas phase (e.g. Lees 2007; Lin et al., 2013; Vargas et al., 2017; Koulakov et al., 2020). On the other hand, a high V_p may be interpreted as an old solidified intrusion/magma chamber, and the corresponding high V_p/V_s may be interpreted as over-pressurized fluids and/or faults (e.g. Feuillet et al., 2004). Anomaly 5 (~10 km) is marked by low V_s , high V_p/V_s ratio (up to 1.8), and no significant variation of the P velocities. Depths of anomalies 2 and 5 coincide with two reservoirs identified by Berthod et al. (2021) through geobarometric analysis on clinopyroxene of dredges made on the NVE in 2019. Berthod et al. (2021) identified a large reservoir at $36.8 - 48.0 \pm 10$ km depth and a smaller reservoir, with a maximum depth of 17.1 ± 6.5 km. Their large reservoir may correspond to our anomaly 2 (~44 km depth), and their smaller reservoir may correspond to anomaly 5 (~10 km depth). From our analysis, anomaly 2 can be interpreted as an old solidified intrusion that is still in use as a reservoir, whereas anomaly 5 could be a shallower reservoir. However, we cannot exclude that anomaly 5 does not present variation in the P velocity model and that it could be located above 10 km. At that depth, the ray geometry induced a decrease of the general resolution and station corrections may have an influence. The coincidence with anomaly 5 and other studies will need further investigation, such as local active tomography, to learn more about the volcanic plumbing near the NVE. We consequently rename anomalies 2 as reservoir A and anomaly 5 as hypothetical reservoir C.

From earthquake locations, Lavayssière et al. (2020) relocated events in the PSC cluster, and this seismicity well delineates reservoirs A and B with an hourglass shape. As stated in Lavayssière et al. (2020), the seismicity could be correlated with the inflation and deflation of the magma reservoirs due to fluid migrations. Because of the high amount of gas at the NVE and HS (Feuillet et al., 2021), we cannot exclude that a part of the seismicity may be attributed to fracturing due to high pressure on magma reservoirs. A similar interpretation was made for the Nevado del Ruiz volcano, for example (Vargas et al. 2017). The presence of gas



may consequently explain the low V_p/V_s ratio in these areas (report to 4.3).

Fig. 9. Overview and scheme of the volcanic plumbing system offshore East Mayotte. A: Scheme of features interpreted from the passive tomography. Red arrow: magmatic fluids potential feeding paths. Blue arrow: gas escape to seafloor and water column. Green arrow: ongoing magmatic eruption path. The green to brown shaded structure highlights old volcanic crystallized paths. Moho depth is from Dofal et al. (2018). HS: Horse Shoe. NVE: New volcanic edifice. Numbers from 1 to 6 and letters from A to C are anomalies described in Section 3 and 4. Degassing at the HS and NVE is from Feuillet et al. (2021) and REVOSIMA reports. The white masked area indicates areas that are not well resolved or not at all resolved. B: V_p/V_s 3D view from the top of the volcanic plumbing system highlighted by an isosurface equal to 1.71. The letter C indicates the Crown structure position. C: same as B with a view of the system from the South.

4.3. Reservoirs interactions

According to previous GNSS modeling (e.g. Lemoine et al, 2020), a deep deflation at 30 km East of Mayotte and at 30 km depth and below was identified. This deflation related to our new seismic imagery support the idea of magmatic fluids being transferred from the PSC

region. Events in the DSC have been relocated and partially highlight a fluid pathway between reservoirs A and C, toward the NVE (Lavayssiere et al., 2020). This path was expected by Berthod et al. (2021) and proposed by Feuillet et al. (2021), Cesca et al. (2020), and Laurent et al. (2020). However, the lack of seismicity at that depth or below the expected fluid pathway makes it impossible to recover the pathway using passive local tomography. Since autumn 2020, seismicity has increased in the DSC, even though overall the seismicity rate in the region has decreased (REVOSIMA, October and November reports). The reports indicate that the increase of seismicity in the DSC delineates a dipping structure between 40-50 km depth that links to the PSC. As the eruption at the NVE is still ongoing, this seismic activity is one more clue to the hypothesis that a path between reservoir A and the NVE exists (green arrow on figure 9). These earthquakes will be used further for a new updated tomography and hopefully will increase the resolution near the NVE.

Cesca et al. (2020) proposed that VLFs events (also known as VLP, for Very Long Period) are the result of the interaction of the seismic wave with a fluid-filled crack or conduit at a depth of 37 ± 11 km. On the other hand, Laurent et al. (2020) relocated VLFs to be between 10 and 30 km depths. In both cases, VLFs are likely linked with fluid migrations and/or resonance (Chouet, 1985; Kumagai et al., 2003; Talandier et al., 2016). Laurent et al. (2020) specified that depending on the depth, the VLFs could be related to magma motion or hydrothermal fluids. Two hypothesis remain here. One hypothesis is the existence of a deep hydrothermal circulation along preexisting faults. Indeed, the PSC seismicity is thought to use pre-existing subvertical faults (Jacques et al. 2019), reactivated by the depletion of reservoir A as observed during caldera collapse (Feuillet et al., 2021). The pre-existing sub vertical faults may be used for hydrothermal circulation. A second hypothesis is that VLFs, ranging between 10 to 30 km, highlight gas transport along pre-existing faults or conduits from reservoir B to the HS area (blue arrow on figure 9). In fact, Berthod et al. (in press) identified the presence

of a shallow reservoir, after dredging the HS region, storing phonolitic magma derived from differentiation of basanite. If we made the hypothesis that this reservoir may correspond to our reservoir B, a potential re-injection of basanitic magma (less viscous) into the reservoir could be responsible for degassing observed at HS. Such large degassing from basanite-phonolite magmas has been observed in the Canary Islands (Tenerife, Edgar et al., 2007) and at Erebus volcano (Oppenheimer et al. 2009). Our results better support the latter hypothesis that will be discussed in the next section.

4.4. Gas storage?

The V_p/V_s ratio parameter is mainly informative, as it is highly sensitive to the presence of liquid and gas. The HS area is known for its gas emission. In December 2019, 3 gas acoustic plume sites were identified, some of them reaching 1000 m high in the water column (Feuillet et al., 2021). Below the HS structure we identified a low V_p/V_s region (~ 1.5), with a minimum ratio of 1.44 accompanied by low V_p (anomaly 3). Low V_p/V_s ratio of about 1.5 and low V_p could be characteristic of over-pressured gas-filled rocks (Koulakov et al 2020; Kuznetsov et al. 2017). Indeed, at the Campi Flegrei volcano (De Siena et al., 2010; Chiarabba and Moretti, 2006), a V_p/V_s ratio lower than 1.5 and low V_p were linked to observed degassing at the surface and interpreted as gas-saturated rock. Similar observations have been made at Yellowstone caldera (e.g. Husen et al., 2004), Naruko volcano (Nakajima and Hasegawa, 2003), Mount Spurr (Koulakov et al., 2013) and the Nevado del Ruiz volcano (Vargas et al., 2017). According to Kuznetsov et al. (2017), if a porous medium is saturated by dry gas, it will act like a sponge and will have a low compression modulus. This would lead to very low V_p , which is exactly what we observed under the HS structure (figures 8, 9). We cannot exclude the possibility of sea water infiltration that may reduce the V_p/V_s ratio (Koulakov et al., 2020). However, because of no V_s variation in the model and because of its location above 10

km depth, even if this anomaly is recovered by synthetic test, we cannot exclude the existence of an artifact. Moreover, station corrections may have an influence. The coincidence of anomaly 3 and the degassing HS should be investigated in future studies to understand the role and the effect of each parameter: potential gas saturated rock existing below the HS and/or sea water infiltrations.

4.5. Role of the inheritance

As indicated at the beginning of this section, we consider that everything higher than the local V_p/V_s average is an anomaly (>1.66). Using a V_p/V_s ratio isocontour equal to 1.69 and 1.71 on figures 8 and 9 (B, C) respectively, we imaged conduits with several branches linking the two reservoirs A and B and the hypothetical reservoir C. The corresponding dV_p and dV_s are heterogeneous, with mainly low dV_s and high or low dV_p . Some of the paths that trend toward the surface coincide with bathymetric volcanic mounts, such as HS (figure 8, FF', anomaly 6) but are weak and further study is needed. In addition, some of the branches at 25 km depth are aligned in a NW-SE direction (along the N130° ridge, figure 7) and with sea bottom eruption sites (figure 1). These paths could reflect cracks in accordance with the immature right-lateral wrenching of the lithosphere (Feuillet et al., 2021) or old crystallized conduits. We could also consider a combined hypothesis of an old fracture zone where few fractures may be used by previous magmatic fluids that are now crystallized like in the N130° volcanic ridge. This is our preferred interpretation. Indeed, Feuillet et al. (2021) noted that the N130° volcanic ridge offshore, East of Mayotte has the same orientation as other volcanic features located northeast of Mayotte and around the Comoros islands. These features - dykes, vent alignments, and rift zones - are arranged in a left-lateral en-echelon structure similar to extensional tectonic structures undergoing oblique extension. In this configuration, Feuillet et al. (2021) inferred that the N130° Mayotte volcanic ridge results from volcanism and tectonic

influences. This extensional structure results from a wide E-W striking zone that transfers strain between the East African rift and the Madagascar grabens (Feuillet et al., 2021). Such a structure may induce high-permeability fracture zones that can be used for magma storage, i.e. magmatic reservoirs. These fracture zones are likely imaged as the N130° low Vs and Vp/Vs anomaly at 25 km depth in our 3D model. Considering the 3 potential reservoirs we have also imaged, these fractures may be used for magma transport and could now be crystallized (green to brown shaded structure in figure 9). Such old conduits have been imaged at the Atka volcanic complex (Koulakov et al., 2020) and Gorely volcano in Kamtchatka (Kuznetsov et al. 2017). We note that some of the conduits we identified stem eastward, in the NVE direction (segment ABC, figure 8). However, we do not have the resolution below the NVE to clearly image this connection.

5. Conclusion

We calculated the first 3D velocity models offshore East Mayotte (110 x 90 x 70 km³) using earthquakes recorded between February and November 2019, resulting from the seismic-volcanic crisis that struck Mayotte since May 2018. We used 3,699 events with 45,359 P and 39,667 S phases, recorded on 70 onshore and offshore stations. The passive tomography used for this study highlights for the first time the old East Mayotte plumbing system, deeply entrenched into the mantle, whose heart seems to be located below the HS area. The results also indicate magmatic materials and fractures induced an overall decrease of P and S velocity in the crust and the mantle.

Considering reservoirs A and B, low Vs and high Vp/Vs areas may be interpreted as magma reservoirs more or less consolidated/old (anomalies 1, 2 respectively), with the presence of melt, mush, and/or fluids. The variations in the Vp model related to reservoirs A and B may be associated with the amount of fluid saturation, crack density, thermal properties,

and lithology (Lees, 2007). Indeed, the percentage of melt may explain the difference between A and B. Vp variation could also be due to differences in the nature of the magma product, where reservoir B may present partial melt and mush of a more evolved phonolitic magma (Berthod et al., in press). Reservoir B could also be the source of volcanism below the HS. On the other hand, reservoir A may be a more primitive magma, directly feeding the NVE. The reservoirs are connected by several fractures and/or old crystallized conduits, whose existence could have been influenced by the regional strain. The overall spatial distribution of the volcanic plumbing system, and mainly the structures aligning in a N120° direction parallel to sea bottom volcanic materials, seems to be clearly controlled by pre-existing fracture zones deeply entrenched in the lithosphere and accompanied by a deep seismicity (Feuillet et al., 2021; Berthod et al., 2021; Lemoine et al., 2020; Cesca et al., 2020; Tzevahirtzian et al., 2021). These pre-existing fracture zones may be influenced by the immature right-lateral wrenching of the lithosphere between the Lwandle and Somalian plates proposed by Famin et al. (2020) and Feuillet et al. (2021). At the end, more investigation should be conducted, such as active tomography, to understand more clearly the first kilometers of the crust and to determine the existence, or not, of anomaly 3, 5 (hypothetical reservoir C) and 6. We note that we were not able to clearly image the NVE connections to other reservoirs or conduits due to lack of resolution in that part of the study area. We observe here a connection between the mantle and the crust that feeds the system, similar to what has been observed at Toba volcano (e.g. Masturyono et al., 2001).

Our study gives a physical/structural image of the volcanic plumbing. It provides a context for other disciplines and future studies, and acts as a baseline for the current state of the system. There are several additional studies that are needed to improve our understanding of this volcanic plumbing system. For instance, an attenuation model should be investigated as it is sensitive to rock temperature and can change by several orders of magnitude if there is

a presence of melt (e.g. Lees 2007). Moreover, local active tomography can provide a clearer assessment of what kind of material and how much is present under the NVE, as well as below the HS, where degassing is occurring closer to Petite Terre, and where past volcanic eruptions have been identified (Feuillet et al., 2021).

Authors contributions

Océane Foix: Conceptualization, Methodology, Software, Validation, Data Curation, Writing – Original Draft, Writing - Review & Editing and Visualization. **Christy Aiken:** Conceptualization, Software, Writing - Review & Editing, Supervision and Funding Acquisition (post-doctoral position). - **Jean-Marie Saurel:** Resources, Software, Writing - Review & Editing. **MAYOBS/REVOSIMA Seismology Group:** Resources, the group manually picked more than 4,000 earthquakes and cleaned the data base. **Nathalie Feuillet, Stephan J. Jorry, Emmanuel Rinnert and Isabelle Thincq:** Resources (as PIs of the MAYOBS oceanographic cruises), Writing - Review & Editing and Funding Acquisition (which notably allowed the OBS data acquisitions).

Acknowledgements

We would like to express our gratitude to all people who contributed to the acquisition of this spectacular data set. Instrument deployment and research oceanographic MAYOBS cruises and Tellus Mayotte project has been funded by the CNRS (National Scientific Research Agency), MI (Interior Ministry), MOM (Overseas Territory Ministry) and MTE (Environment Ministry), MESRI (Higher Education, Research and Innovation Ministry) MINARM (Armed Forces Ministry). MAYOBS oceanographic campaigns were conducted with the help and collaborations of French research institutions: Institut de Physique du Globe de Paris (IPGP), BRGM-French geological survey, and Institut Français de Recherche pour l'Exploitation de la

Mer (IFREMER). We thank the help and collaboration of the Genavir technicians and engineers. We want to thank the crew of R/V Marion Dufresne (TAAF/IFREMER/LDA) and their Captains A.Eyssautier and F.Landreau. Since the beginning of the crisis, several seismic stations have been deployed by several person that we would like to thanks here: Didier Bertil, Alison Colombain, Maxime Bès de Berc, Marc Grunberg, Christophe Sira, Antoine Schlupp, Jérôme van der Woerd, Céleste Broucke, Hélène Jund, Grégoire Dectot, Aline Peltier and Philippe Kowalski. For the OBS deployment, we thank Romuald Daniel, Simon Besançon, Wayne Crawford and Jérémy Gomez and Pascal Pelleau, Pierre Guyavarch, Mickaël Roudault, Emmanuel Maros and Pascal Pelleau. We also would like to say our gratitude to the REseau VOlcanologique et Sismologique de MAyotte (REVOSIMA) for the multiple exchanges and to IFREMER scientific direction for funding the postdoctoral position. The figures of the paper were produced using Generic Mapping Tool (Wessel et al., 2013), Adobe Illustrator, Surfer 11 and Voxler Golder Softwares, as well as Python, Matlab and Microsoft Excel. We are grateful to the reviewers for their constructive comments.

Supplementary data

Supplementary material

References

- Audru J. C., Guennoc P., Thinon I., and Abellard O., (2006). Bathymay : la structure sous-marine de Mayotte révélée par l'imagerie multifaisceaux. *Comptes Rendus - Geoscience*, 338(16), 1240–1249.
<https://doi.org/10.1016/j.crte.2006.07.010>
- Barruol G., Sigloch K., Scholz J.-R., Mazzullo A., Stutzmann E., Montagner J.-P., Kiselev S., Fontaine F. R., Michon L., Deplus C., Dymont, J. (2019). Large-scale flow of Indian Ocean asthenosphere driven by Réunion plume. *Nat. Geo.*, 12, 1043-1049. <https://doi.org/10.1038/s41561-019-0479-3>
- Bazin S., Feuillet N., Duclos C., Crawford W., Nercessian A., Bengoubou-Valérius M., Beauducel F., Singh S.C., (2010). The 2004-2005 Les Saintes (French West Indies) seismic aftershock sequence observed

- 669 with ocean bottom seismometers. *Tectonophysics*, 498, 91-103
- 670 Berthod C., Médard E., Bachèlery P., Gurioli L., Di Muro A., Peltier A., Komorowski J.C., Benbakkar M.,
 671 Devidal J.-L., Langlade J., Besson P., Boudon G., Rose-Koga E., Deplus C., Le Friant A., Bickert M.,
 672 Nowak S., Thinon I., Burckel P., Hidalgo S., Kaliwoda M., Jorry S.J., Fouquet Y., Feuillet N., (2021).
 673 The 2018-ongoing Mayotte submarine eruption: 1 magma migration imaged by petrological monitor-
 674 ing. *Earth and Planetary Science Letters*, 571. <https://doi.org/10.1016/j.epsl.2021.117085>
- 675 Berthod C., Médard E., Di Muro A., Hassen Ali T., Gurioli L., Bachèlery P., Komorowski J.-C., Laporte D.,
 676 Peltier A., Benbakkar M., Devidal J.-L., Langlade J., Besson P., Rose-Koga E., Deplus C., Le Friant A.,
 677 Bickert M., Nowak S., Thinon I., Burckel P., Hidalgo S., Feuillet N., Jorry S.J., Fouquet Y., (in press).
 678 Mantle xenolith-bearing phonolites feeding the active volcanic ridge of Mayotte (Comoros archipelago,
 679 Mozambique Channel). *Contribution to Mineralogy and Petrology* [https://doi.org/10.1007/s00410-021-](https://doi.org/10.1007/s00410-021-01833-1)
 680 [01833-1](https://doi.org/10.1007/s00410-021-01833-1)
- 681 Bertil D., Roullé A., Lemoine A., Colombain A., Maisonhaute E and Dectot G, (2018). MAYEQSwarm2018 :
 682 BRGM earthquake catalogue for the Earthquake Swarm located East of Mayotte, May 10th -November
 683 12th, 2018. <https://doi.org/10.18144/372c08c9-3c30-440c-b44a-1c89385f176a>
- 684 Cesca S., Letort J., Razafindrakoto H.N.T., Heimann S., Rivalta E., Isken M.P., Nikkhoo M., Passarelli L., and
 685 Petersen G.M., (2020). Drainage of a deep magma reservoir near Mayotte inferred from seismicity and
 686 deformation. *Nat. Geo.* 13(January). <https://doi.org/10.1038/s41561-019-0505-5>
- 687 Chiarabba, C. and Moretti, M. (2006). An insight into the unrest phenomena at the Campi Flegrei caldera from
 688 Vp and Vp/Vs tomography. *Terra Nova*, 18: 373-379. [https://doi.org/10.1111/j.1365-](https://doi.org/10.1111/j.1365-3121.2006.00701.x)
 689 [3121.2006.00701.x](https://doi.org/10.1111/j.1365-3121.2006.00701.x)
- 690 Chouet B., (1985). Excitation of a buried magmatic pipe: a seismic source model for volcanic tremor. *J. Ge-*
 691 *ophys. Res.* 90, 1881–1893. <https://doi.org/10.1029/JB090iB02p01881>
- 692 Darnet M., Wawrzyniak P., Tarits P., Hautot S., and D'Eu J. F., (2020). Mapping the geometry of volcanic sys-
 693 tems with magnetotelluric soundings: Results from a land and marine magnetotelluric survey performed
 694 during the 2018–2019 Mayotte seismovolcanic crisis. *Journal of Volcanology and Geothermal Re-*
 695 *search*, 406, 107046.
- 696 Debeuf D., (2004). Etude de l'évolution volcano-structurale et magmatique de Mayotte, Archipel des Comores,
 697 océan Indien: approches structurales, pétrographique, géochimique et géochronologique, PhD, La Réu-
 698 nion University, 277p

- 697 De Natale G., Troise C., Trigila R., Dolfi D., Chiarabba C., (2004). Seismicity and 3D substructure at Somma–
 698 Vesuvius volcano: evidence for magma quenching. *Earth Planet. Sci. Lett.*, 221, 181–196,
 699 [https://doi.org/10.1016/S0012-821X\(04\)00093-7](https://doi.org/10.1016/S0012-821X(04)00093-7)
- 700 De Siena L., Del Pezzo E., Bianco F., (2010). Seismic attenuation imaging of Campi Flegrei: Evidence of gas
 701 reservoirs, hydrothermal basins, and feeding systems. *J. Geophys. Res. Solid Earth*, 115(B9).
 702 <https://doi.org/10.1029/2009JB006938>
- 703 Deville E., Marsset T., Courgeon S., Jatault R., Ponte J.P., Thereau E., Jouet G., Jorry S. J., Droz L., (2018).
 704 Active fault system across the oceanic lithosphere of the Mozambique Channel: Implications for the
 705 Nubia–Somalia southern plate boundary. *Earth Planet. Sci. Lett.*, 507, 210–220.
 706 <https://doi.org/10.1016/j.epsl.2018.08.052>
- 707 Dobretsov N.L., Koulakov I.Y., and Litasov, Y.D., (2012). Migration paths of magma and fluids and lava com-
 708 positions in Kamchatka. *Russian Geology and Geophysics*, 55(12), 1253–1275.
 709 <https://doi.org/10.1016/j.rgg.2012.10.001>
- 710 Dofal A., Fontaine F.R., Michon L., Barruol G., and Tkalic H. (2018). Crustal structure variation across the
 711 southwestern Indian Ocean from receiver functions determined at Ocean-Bottom Seismometers. AGU
 712 Fall Meeting, Abstract ID T43G0497B
- 713 Edgar C.J., Wolff J.A., Olin P.H., Nichols H.J., Pitarri A., Cas R.A.F., Reiners P.W., Spell T.L., Martí J., (2007).
 714 The late Quaternary Diego Herrero Formation, Tenerife: volcanology of a complex cycle of volumi-
 715 nous explosive phonolitic eruptions. *J. Volcanol. Geotherm. Res.* 160, 59–85.
 716 <https://doi.org/10.1016/j.jvolgeores.2006.06.001>
- 717 Emerick C.M., and Duncan R. A., (1982). Age progressive volcanism in the Comores Archipelago, eastern Indi-
 718 an Ocean and implications for Somali plate tectonics. *Earth Planet. Sci. Lett.* 60(3), 415–428.
 719 [https://doi.org/10.1016/0012-821X\(82\)90077-2](https://doi.org/10.1016/0012-821X(82)90077-2)
- 720 Famin V., Michon L. and Bourhane A., (2020). The Comoros archipelago: a right-lateral transform boundary
 721 between the Somalia and Lwandle plates. *Tectonophysics* 789-228539.
 722 <https://doi.org/10.1016/j.tecto.2020.228539>
- 723 Feuillet N., Nostro C., Chiarabba C., Cocco M, (2004). Coupling between earthquake swarms and volcanic un-
 724 rest at the Alban Hills Volcano (central Italy) modeled through elastic stress transfer. *Journal of Geo-*
 725 *physical Research* Vol. 109, B02308. <https://doi.org/10.1029/2003JB002419>
- 726 Feuillet N., Jorry S.J., Rinnert E., Thinon I., Fouquet Y., (2019). MAYOBS. <https://doi.org/10.18142/291>

- 755 Feuillet N., Jorry S.J., Crawford W.C., Deplus C., Thimon I., Jacques E., Saurel J.-M., Lemoine A., Paquet F.,
 756 Daniel R., Gaillot A., Satriano C., Peltier A., Aiken C., Foix O., Kowalski P., Laurent A., Beauducel F.,
 757 Grandin R., Ballu V., Bernard P., Donval J.-P., Géli L., Gomez J., Pelleau P., Guyader V., Rinnert E.,
 758 Besançon S., Bertil D., Lemarchand A., Vanderwoerd J., (2021). Birth of a large volcanic edifice
 759 through lithosphere-scale dyking offshore Mayotte (Indian Ocean). *Nature Geoscience*.
 760 <https://doi.org/10.1038/s41561-021-00809-x>
- 761 Hamada, (2004). Reservoir Fluids Identification Using Vp/Vs Ratio. *Oil & Gas Science and Technology – Rev.*
 762 *IFP*, Vol. 59, No. 6, pp. 649-654. <https://doi.org/10.2516/ogst:2004046>
- 763 Husen S., Smith R.B., Waite G.P., (2004). Evidence for gas and magmatic sources beneath the Yellowstone vol-
 764 canic field from seismic tomographic imaging. *J. Volcanol. Geotherm. Res.*, 131, 397–410.
 765 [https://doi.org/10.1016/S0377-0273\(03\)00416-5](https://doi.org/10.1016/S0377-0273(03)00416-5)
- 766 Jacques E., Feuillet N., Aiken C., Lemoine A., Crawford W.C., Deplus C., Thimon I., Saurel J.-M., Bès de Berc
 767 M., Broucke C., Colombain A., Daniel R., Dectot G., Foix O., Gomez J., Grunberg M., Kow-
 768 alski P., Laurent A., Léger F., Lemarchand A., and Pelleau P., (2019). The 2018-2019 Mayotte Seismic
 769 Crisis: Evidence of an upper Mantle Rifting Event? AGU Fall Meeting, V43I-0221
- 770 Kennett B., Engdahi E., and Buland R., (1995). Constraints on seismic velocities in the earth from travel times.
 771 *Geophys. J. Int* 122, 108–124. <https://doi.org/10.1111/j.1365-246X.1995.tb03540.x>
- 772 Koulakov I., and Sobolev S. V., (2006). A tomographic image of Indian lithosphere break-off beneath the Pamir-
 773 Hindukush region. *Geophys. J. Int.*, 164(2), 425–440. <https://doi.org/10.1111/j.1365-246X.2005.02841.x>
- 774 Koulakov I., (2009). LOTOS Code for Local Earthquake Tomographic Inversion: Benchmarks for Testing
 775 Tomographic Algorithms. *Bulletin of the Seismological Society of America*, 99(1), 194–214.
 776 <https://doi.org/10.1785/0120080013>
- 777 Koulakov I., Yudistira T., Luehr B.G., and Wandono X., (2009a), P, S velocity and VP/VS ratio beneath the
 778 Toba caldera complex (northern Sumatra) from local earthquake tomography, *Geophys. J. Int.*, 177,
 779 1121–1139. <https://doi.org/10.1111/j.1365-246X.2009.04114.x>
- 780 Koulakov I., West M., Izbekov P., (2013). Fluid ascent during the 2004–2005 unrest at Mt. Spurr inferred from
 781 seismic tomography. *Geophys. Res. Lett.*, 40, 4579–4582. <https://doi.org/10.1002/grl.50674>
- 782 Koulakov I., Boychenko E., and Smirnov S. Z., (2020). Magma Chambers and Meteoric Fluid Flows Beneath
 783 the Atka Volcanic Complex (Aleutian Islands) Inferred from Local Earthquake Tomography. *Geosci-*

- 784 ences 10, 214. <https://doi.org/10.3390/geosciences10060214>
- 785 Koulakov I., Shapiro N.M., Sens-Schönfelder C., Luehr B.G., Gordeev E.I., Jakovlev A., Abkadyrov I., Chebrov
 786 D.V., Bushenkova N., Droznina S.Y., Senyukov S.L., Novgorodova A., and Stupina T., (2020a). Man-
 787 tle and crustal sources of magmatic activity of Klyuchevskoy and surrounding volcanoes in Kamchatka
 788 inferred from earthquake tomography. *Journal of Geophysical Research: SolidEarth*.
 789 <https://doi.org/10.1029/2020JB020097>
- 790 Kumagai H., Miyakawa K., Negishi H., Inoue H., Obara K., Suetsugu D., (2003). Magmatic dyke resonances
 791 inferred from very-long-period seismic signals. *Science* 299, 2058–2061.
 792 <https://doi.org/10.1126/science.1081195>
- 793 Kuznetsov P., Koulakov I., Jakovlev A., Abkadyrov I., Deev E., Gordeev E., Senyukov S., El Khrepy S., Al Ari-
 794 fi N., (2017). Structure of Volatile Conduits Beneath Gorely Volcano (Kamchatka) Revealed by Local
 795 Earthquake Tomography. *Geosciences* 2017, 7, 111. <https://doi.org/10.3390/geosciences7040111>
- 796 Lavayssière A., Crawford W., Saurel J.M., Satriano C., Komorowski J.-C., MAYOBS/REVOSIMA Seismology
 797 Group, (2020). New 1D velocity model and absolute locations image of Mayotte seismo-volcanic re-
 798 gion. AGU Fall Meeting - V019-724062
- 799 Laurent A., Satriano C., and Bernard P., (2020). Detection, location and characterization of VLF events during
 800 the 2018-2019 seismovolcanic crisis in Mayotte. HAL Archive Ouvertes. [https://hal.archives-](https://hal.archives-ouvertes.fr/hal-02446050)
 801 [ouvertes.fr/hal-02446050](https://hal.archives-ouvertes.fr/hal-02446050)
- 802 Lees J.M., and Crosson R.S., (1989). Tomographic inversion for three-dimensional velocity structure at Mount
 803 St. Helens using earthquake data. *J. Geophys. Res.*, 94(B5), 5716–5728.
 804 <https://doi.org/10.1029/JB094iB05p05716>
- 805 Lees J.M., (2007). Seismic tomography of magmatic systems. *J. Volcanol. Geotherm. Res.*, 167, 37–56.
 806 <https://doi.org/10.1016/j.jvolgeores.2007.06.008>
- 807 Lemoine A., Briole P., Bertil D., Roullé A., Foumelis M., Thinon, I., Raucoules D., de Michele M., Valtý P.,
 808 and Hoste Colomer R., (2020). The 2018-2019 seismo-volcanic crisis east of Mayotte, Comoros is-
 809 lands : seismicity and ground deformation markers of an exceptional submarine eruption. *Geophys. J.*
 810 *Int.* 223, 22–44. <https://doi.org/10.1093/gji/ggaa273>
- 811 Lin G., Shearer P.M., Matoza, Okubo P.G., and Amelung F., (2013). Three-dimensional seismic velocity struc-
 812 ture of Mauna Loa and Kilauea volcanoes in Hawaii from local seismic tomography. *J. Geophys. Res.*
Solid Earth, 119, 4377–4392. <https://doi.org/10.1002/2013JB010820>

- 813 Masson F., Sira C., Schlupp A., Bontemps M., Regis E., Bertil D., Lemoine A., Roll A., Tronel F., van der
 814 Woerd J., (2018). Note macrosismique préliminaire du BCSF-RENASS.
 815 http://www.franceseisme.fr/donnees/Note_macro-BCSF-RENASS-Mayotte-13-07-2018.pdf
- 816 Masturyono, McCaffrey R., Wark D.A., Roecker S.W., Fauzi G., Sukhyar I., (2001). Distribution of magma be-
 817 neath Toba Caldera, North Sumatra, Indonesia, constrained by 3Dimensional P-wave velocities, seis-
 818 micity, and gravity data. *Geochem. Geophys. Geosyst.* 2 (4). <https://doi.org/10.1029/2000GC000096>
- 819 Michon, L., (2016). The Volcanism of the Comoros Archipelago Integrated at a Regional Scale. In : Active Vol-
 820 canoes of the Southwest Indian Ocean, Active Volcanoes of the World. P. Bachelery et al (Eds.).
- 821 Nakajima J., Matsuzawa T., Hasegawa A., Zhao D., (2001). Three-dimensional structure of Vp, Vs, and Vp/Vs
 822 beneath northeastern Japan: Implications for arc magmatism and fluid. *J. Geophys. Res.*, 106(B10),
 823 21843– 21857. <https://doi.org/10.1029/2000JB000008>
- 824 Nakajima J., Hasegawa A., (2003). Tomographic imaging of seismic velocity structure in and around the Oniko-
 825 be volcanic area, northeastern Japan: Implications for fluid distribution. *J. Volcanol. Geotherm. Res.*,
 826 127, 1–18. [https://doi.org/10.1016/S0377-0273\(03\)00055-0](https://doi.org/10.1016/S0377-0273(03)00055-0)
- 827 Nougier J., Cantagrel J.M., and Karche J.P., (1986). The Comores archipelago in the western Indian Ocean: vol-
 828 canology, geochronology and geodynamic setting, *J. African Earth Sci.*, 5(2), 135-144.
 829 [https://doi.org/10.1016/0899-5362\(86\)90003-5](https://doi.org/10.1016/0899-5362(86)90003-5)
- 830 Oppenheimer C., Lomakina A.S., Kyle P.P., Kingsbury N.G., Boichu M., (2009). Pulsatory magma supply to a
 831 phonolite lava lake. *Earth Planet. Sci. Lett.*, 284, 392–398. <https://doi.org/10.1016/j.epsl.2009.04.043>
- 832 Paige C., Saunders M.A., (1982). LSQR: an algorithm for sparse linear equations and least squares problems.
 833 *ACM Trans. Math. Soft.*, 8, 43-71.
- 834 Phethean J.J.J., Kalnins L.M., van Hunen J., Biffi P.G., Davies R.J., McCaffrey K.J.W., (2016). Madagascar's
 835 escape from Africa: A high-resolution plate reconstruction for the Western Somali Basin and implica-
 836 tions for supercontinental dispersal. *Geochemistry, Geophysics, Geosystems*, 17(12), 5036-5055,
 837 <https://doi.org/10.1002/2016GC006624>.
- 838 Saurel J.-M., Jacques E., Aiken C., Lemoine A., Retailleau L., Lavayssière A., Foix O., Laurent A., Mercury N.,
 839 Crawford W., Lemarchand A., Daniel R., Pelleau P., Bès de Berc M., Dectot G., Bertil D., Roulle A.,
 840 Broucke C., Colombain A., Besançon S., Guyavarch P., Kowalski P., Roudaut M., Battaglia J., Bodihar
 841 S., Bouin M.P., Canjamale K., Desfete N., Dofal A., Doubre C., Dretzen R., Ferrazzini V., Fontaine F.,
 Géli L., Griot C., Grunberg M., Guzel E.C., Hoste-Colomer R., Lambotte S., Léger F., Vergne J.,

- Satriano C., Tronel F., Vanderwoerd J., Feuillet N., Fouquet Y., Jorry S.J., Rinnert E., and Thinon I., (resubmitted to *Geophys. J. Int.*). Mayotte seismic crisis: building knowledge in near real-time combining land and ocean-bottom seismometers, first results.
- Stamps D.S., Kreemer C., Fernandes R., Rajaonarison T.A., and Rambolamanana G., (2020). Redefining East African Rift System kinematics. *Geology*, 49, 150-155. <https://doi.org/10.1130/G47985.1>
- Talandier J., Hyvernaud O., Maury R. C., (2016). Unusual seismic activity in 2011 and 2013 at the submarine volcano Rocard, Society hot spot (French Polynesia). *Geophys. Res. Lett.* 43(9).
<https://doi.org/10.1002/2016GL068342>
- Thinon I., Leroy S., Lemoine A.; (2020) SISMAORE cruise, RV Pourquoi pas?,
<https://doi.org/10.17600/18001331>
- Tzevahirtzian A., Zaragosi S., Bachèlery P., Biscara L., Marchès E., (2021) Submarine morphology of the Comoros volcanic archipelago. *Marine Geology*, 432. <https://doi.org/10.1016/j.margeo.2020.106383>
- Vargas C.A., Koulakov I., Jaupart C., Gladkov V., Gomez E., El Karaby S., Al-Arifi N., (2017). Breathing of the Nevado del Ruiz volcano reservoir, Colombia, inferred from repeated seismic tomography. *Sci. Rep.*, 7, 46094. <https://doi.org/10.1038/srep46094>
- Wessel P., Smith W. H. F., Scharroo R., Luis J., Wobbe F., (2013). Generic Mapping Tools: Improved Version Released. *EOS Trans. AGU*, 94(45), 409–410. <https://doi.org/10.1002/2013EO450001>
- Zelt C. A., and Barton P. J., (1998). Three-dimensional seismic refraction tomography: A comparison of two methods applied to data from the Faeroe Basin. *Journal of Geophysical Research: Solid Earth*, 103(B4), 7187–7210. <https://doi.org/10.1029/97JB03536>
- Zinke J., Reijmer J.J.G., Thomassin B.A., Dullo W.C., Grootes P.M., and Erlenkeuser H., (2003a). Postglacial flooding history of Mayotte lagoon (Comoro archipelago, southwest Indian Ocean). *Marine Geology*, 194(3-4), 181-196. [https://doi.org/10.1016/S0025-3227\(02\)00705-3](https://doi.org/10.1016/S0025-3227(02)00705-3)
- Zinke J., Reijmer J.J.G., and Thomassin B.A., (2003b). Systems tracts sedimentology in the lagoon of Mayotte associated with the Holocene transgression. *Sedimentary Geology*, 160(1-3), 57-79.
[https://doi.org/10.1016/S0037-0738\(02\)00336-6](https://doi.org/10.1016/S0037-0738(02)00336-6)

Declaration of interests

The authors declare that they have no known competing financial interests or personal relationships that could have appeared to influence the work reported in this paper.

The authors declare the following financial interests/personal relationships, which may be considered as potential competing interests:

Author statement: Océane Foix: Conceptualization, Methodology, Software, Validation, Data Curation, Writing – Original Draft, Writing - Review & Editing and Visualization. **Chastity Aiken:** Conceptualization, Software, Writing - Review & Editing, Supervision and Funding Acquisition (post-doctoral position). **Jean-Marie Saurel:** Resources, Software, Writing - Review & Editing. **MAYOBS/REVOSIMA Seismology Group:** Resources: the group manually picked more than 4,000 earthquakes and cleaned the data based. **Nathalie Feuillet, Stephan J. Jorry, Emmanuel Rinert and Isabelle Thainon:** Resources (as PIs of the MAYOBS oceanographic cruises), Writing - Review & Editing and Funding Acquisition (which notably allowed the OBS data acquisitions).

Highlights (< 85 characters) • We calculated the first 3-D velocity models offshore Mayotte that revealed 3 potential magma reservoirs more or less related to the ongoing eruption. • Reservoirs are connected by several crystallized conduits with a spatial distribution constrained by regional strike-slip faulting of the lithosphere in the N130° directions. • A gas saturated area was identified below the *Fer-à-Cheval* structure, known for its presently

degassing acoustic plumes.

Journal Pre-proof